Manipulating L-type calcium channels in cardiomyocytes using split-intein protein transsplicing

Prakash Subramanyam, Donald D. Chang, Kun Fang, Wenjun Xie, Andrew R. Marks, and Henry M. Colecraft[1]

Department of Physiology and Cellular Biophysics, Columbia University, New York, NY 10032

Edited by Kurt G. Beam, University of Colorado at Denver, Aurora, CO, and approved August 6, 2013 (received for review April 30, 2013)

Manipulating expression of large genes (>6 kb) in adult cardiomyocytes is challenging because these cells are only efficiently transduced by viral vectors with a 4–7 kb packaging capacity. This limitation impedes understanding structure–function mechanisms of important proteins in heart. L-type calcium channels (LTCCs) regulate diverse facets of cardiac physiology including excitation–contraction coupling, excitability, and gene expression. Many important questions about how LTCCs mediate such multidimensional signaling are best resolved by manipulating expression of the 6.6 kb pore-forming α_{1C}-subunit in adult cardiomyocytes. Here, we use split-intein–mediated protein transsplicing to reconstitute LTCC α_{1C}-subunit from two distinct halves, overcoming the difficulty of expressing full-length α_{1C} in cardiomyocytes. Split-intein–tagged α_{1C} fragments encoding dihydropyridine-resistant channels were incorporated into adenovirus and reconstituted in cardiomyocytes. Similar to endogenous LTCCs, recombinant channels targeted to dyads, triggered Ca^{2+} transients, associated with caveolin-3, and supported β-adrenergic regulation of excitation–contraction coupling. This approach lowers a longstanding technical hurdle to manipulating large proteins in cardiomyocytes.

CaV1.2 | ventricular myocytes | gene transfer | protein splicing

Adult ventricular cardiomyocytes have a unique cytoarchitecture and intracellular milieu (including transverse tubules, dyadic junctions, and ryanodine receptors) that is not replicated in many other cell types (1). Consequently, many fundamental questions regarding structure–function mechanisms of cardiac signaling proteins can only be pursued in the context of native cardiomyocytes. Knock-in mouse models are unarguably the gold standard for structure–function studies of signaling proteins in heart. However, the high cost (~$50,000) and length of time (up to 2 y) required to generate a single knock-in mouse makes it impractical to routinely use this model system for investigative studies of structure–function mechanisms in heart cells. Directly manipulating expression of target proteins in adult cardiomyocytes is an important tool for structure–function studies in heart (2). However, this approach is challenging because (*i*) adult cardiomyocytes are refractory to transfection using conventional methods and (*ii*) they can only be maintained in culture for short periods (3–4 d) before they dedifferentiate (2). Fortunately, adult cardiomyocytes are efficiently transduced by viral vectors. A major technical hurdle is that commonly used viral vectors have a packaging capacity of 4–7 kb (2, 3).

Studies of the cardiac L-type calcium channel (LTCC) illustrate these challenges. In heart, LTCCs mediate excitation–contraction (EC) coupling, control excitability, and regulate gene expression (1, 4). In ventricular myocytes, the majority of LTCCs are targeted to transverse tubules where they are closely apposed to intracellular Ca^{2+} release channels, ryanodine receptors (RyR2), at dyadic junctions (4, 5) (Fig. 1*A*). This spatial arrangement is critical for the high gain of Ca^{2+}-induced Ca^{2+} release (CICR) that underlies cardiac EC coupling (6). A subset of cardiac LTCCs are found located in caveolae (7), and are hypothesized to selectively signal through local effectors to the nucleus (8, 9) (Fig. 1*A*). Cardiac LTCC currents are increased several-fold by protein kinase A (PKA), which is activated via β-adrenergic signaling (10). The molecular mechanisms and determinants underlying LTCC targeting to dyads and caveolae and modulation by PKA are either unknown or ambiguous. Reconstituting LTCCs in heterologous cells to address such questions has proven inadequate because these cells are deficient in essential structural elements such as transverse (t) tubules (Fig. 1*B*), and also lack a permissive environment for PKA modulation (11, 12). Moreover, because resolving these structure–function questions will likely require many different constructs, it is impractical to use knock-in mice for such investigative purposes. Hence, directly manipulating LTCCs in isolated adult ventricular myocytes is critical for addressing these questions. Cardiac LTCCs are multisubunit proteins containing a pore-forming α_{1C} assembled with auxiliary β and $\alpha_2\delta$ subunits, and calmodulin (13) (Fig. 1*C*). The 6.6 kb size of α_{1C} is at the packaging capacity of commonly used viral vectors, making it difficult to generate viral vectors incorporating full-length α_{1C}. This deficiency has been a major roadblock to progress in determining structure–function mechanisms of cardiac LTCCs.

To overcome the obstacle of routinely expressing LTCC α_{1C} and other large proteins in adult cardiomyocytes, we developed an approach that relies on split-intein–mediated protein transsplicing. Inteins are naturally occurring protein-splicing elements found in archaeal, eubacterial, and eukaryotic genes (14). When attached to two different polypeptides (termed "exteins"), trans-acting split inteins can rapidly associate to form an active intein that uses a self-catalytic reaction to splice the two exteins together with a peptide bond while excising itself out of the resulting protein sequence (15, 16). We used the split DnaE intein from the cyanobacterium *Nostoc punctiforme* (17, 18) to reconstitute full-length α_{1C} in situ from two separate halves. The split-intein–tagged α_{1C} fragments readily incorporated into adenovirus and reconstituted dihydropyridine (DHP)-resistant channels in cardiomyocytes. Similar to endogenous LTCCs, intein-spliced α_{1C} subunits targeted to dyads, triggered Ca^{2+} transients, associated with caveolin-3, and supported PKA regulation of EC coupling.

Significance

Manipulating expression of proteins directly in isolated heart cells is an important method to study cardiac biology and disease. However, this approach is challenging for large genes (>6 kb) because these exceed the packaging capacity of commonly used viral vectors used to deliver genes into heart cells. Here, we used a split-intein–mediated protein transsplicing strategy to reconstitute the large pore-forming subunit of L-type calcium channels from two separate fragments in heart cells. This approach provides a general method to express different large proteins in heart cells and will help advance new insights into basic mechanisms underlying cardiac function and disease.

Author contributions: P.S. and H.M.C. designed research; P.S., D.D.C., K.F., and W.X. performed research; A.R.M. contributed new reagents/analytic tools; P.S. and H.M.C. analyzed data; and P.S. and H.M.C. wrote the paper.

The authors declare no conflict of interest.

This article is a PNAS Direct Submission.

[1]To whom correspondence should be addressed. E-mail: hc2405@columbia.edu.

This article contains supporting information online at www.pnas.org/lookup/suppl/doi:10.1073/pnas.1308161110/-/DCSupplemental.

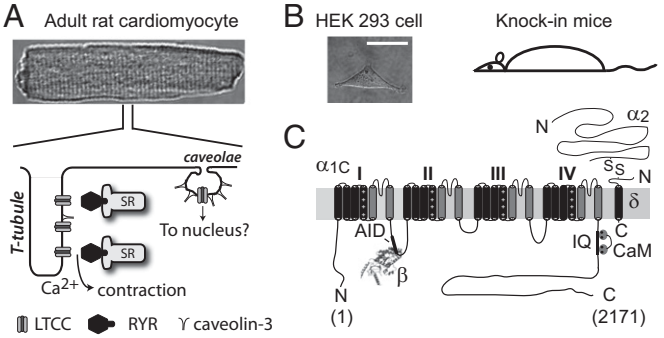

Fig. 1. Model systems for structure–function studies of cardiac LTCCs. (*A*, *Upper*) Adult rat ventricular cardiomyocyte. (*A*, *Bottom*) Differential LTCC targeting to distinct subcellular microdomains in cardiomyocytes. (*B*) Model systems for LTCC structure–function studies. (Scale bar, 20 μm.) (*C*) Topology of LTCC pore-forming α_{1C} and auxiliary proteins (β, α2δ, and calmodulin).

Results

Design and Functional Properties of Split-Intein–Spliced α_{1C} Reconstituted in HEK293 Cells. LTCC α_{1C} subunit is a 2,171-residue protein containing four homologous domains each with six transmembrane segments and cytoplasmic *N* and C termini (19) (Fig. 1*C*). The homologous domains are joined by long intracellular loops. We split α_{1C} cDNA at the II–III loop and cloned the split-intein fragments of *N. punctiforme* DnaE intein into the C and *N* termini of the left ($[I–II]_{N\text{-intein}}$) and right ($_{C\text{-intein}}[III–IV]$) halves, respectively (Fig. 2*A* and Fig. S1). To visualize and distinguish reconstituted channels from endogenous LTCCs, we attached CFP and YFP to the *N* and C termini of $[I–II]_{N\text{-intein}}$ and $_{C\text{-intein}}[III–IV]$, respectively; engineered an extracellular epitope tag (bungarotoxin-binding site, BBS) (20, 21) into domain II S5–S6 loop of $_{CFP}[I–II]_{N\text{-intein}}$; and introduced two mutations (T1066Y/Q1070M) into $_{C\text{-intein}}[III–IV]_{YFP}$ that render LTCCs relatively insensitive to DHP blockers (DHP–) (22, 23) (Fig. 2*A*). When coexpressed in cells, we predicted $_{CFP}[I–II]_{N\text{-intein}}$ and $_{C\text{-intein}}[III–IV]_{YFP}$ would interact to form a spliced α_{1C} intermediate in which the split *N. punctiforme* DnaE inteins associate to form an active intein. The active intein would then use a self-catalyzed reaction to splice the two channel halves together while excising itself out (Fig. 2*A*). Typically, three intein residues—cysteine, phenylalanine, and asparagine—are left behind in the spliced product. Taking advantage of an endogenous asparagine residue at the split site, we designed constructs so that the splicing reaction leaves behind only two foreign residues, cysteine and phenylalanine (Fig. S1).

We first used Western blotting to determine whether coexpression of split-intein–tagged α_{1C} moieties in HEK293 cells resulted in a reconstituted full-length protein as conceptualized in Fig. 2*A*. In cells expressing either $_{CFP}[I–II]_{N\text{-intein}}$ or $_{C\text{-intein}}[III–IV]_{YFP}$ alone, respectively, anti-GFP (which recognizes both CFP and YFP) Western blots revealed bands corresponding to the two half proteins (Fig. 2*B*, lanes 2 and 3). In cells coexpressing $_{CFP}[I–II]_{N\text{-intein}}$ and $_{C\text{-intein}}[III–IV]_{YFP}$, we detected a higher molecular weight band at the expected size of the spliced WT α_{1C} channel product (Fig. 2*B*, lane 4). We similarly detected the spliced DHP-resistant α_{1C} channel when $_{CFP}[I–II]_{N\text{-intein}}$ was coexpressed with $_{C\text{-intein}}[III–IV^{TQ/YM}]_{YFP}$ (Fig. 2*B*, lane 5). The transsplicing reaction was highly efficient, as evidenced by the complete consumption of the moiety with limiting expression ($_{C\text{-intein}}[III–IV]_{YFP}$) in the reaction (Fig. 2*B*, lanes 4 and 5). The high efficiency of the transsplicing reaction is likely aided by the fact that the I–II and III–IV domains of Ca_V channels have a natural affinity for each other and interact when coexpressed (24–26). By titrating the relative amount of $_{CFP}[I–II]_{N\text{-intein}}$ to $_{C\text{-intein}}[III–IV]_{YFP}$ cDNA transfected, it was possible to approach a balanced level of expression where both fragments were essentially used up in the splicing reaction (Fig. 2*C*).

We next determined whether intein-spliced α_{1C} had similar functional properties to full-length (WT) α_{1C} subunit expressed in HEK293 cells. First, WT α_{1C} requires coexpression of $Ca_V\beta$

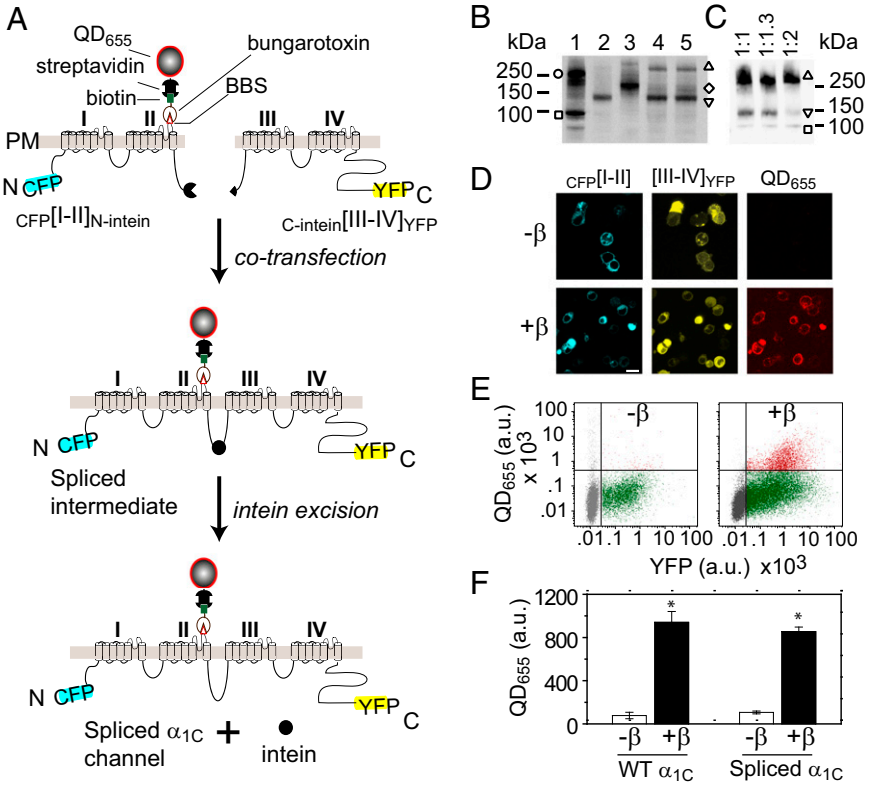

Fig. 2. Reconstituting LTCCs by split-intein–mediated protein transsplicing. (*A*) Strategy for reconstituting full-length α_{1C} using split-intein–mediated protein splicing. The α_{1C} subunit is split into two halves tagged with fluorophores and flanking *N. punctiforme* DnaE split inteins, creating $_{CFP}[I–II]_{N\text{-intein}}$ and $_{C\text{-intein}}[III–IV]_{YFP}$, respectively. A 13-residue BBS tag is introduced to permit selective labeling of surface channels with quantum dot (QD_{655}). (*B* and *C*) Anti-GFP Western blot showing successful reconstitution of covalently linked full-length α_{1C} from intein-flanked α_{1C} moieties in HEK293 cells. Lane 1, full-length α_{1C}[BBS]–YFP (open circle) + β_{2a}-CFP (open square); lane 2, $_{CFP}[I–II]_{N\text{-intein}}$ (inverted triangle); lane 3, $_{C\text{-intein}}[III–IV]_{YFP}$ (open diamond); lane 4, $_{CFP}[I–II]_{N\text{-intein}}$ + $_{C\text{-intein}}[III–IV]_{YFP}$ (open triangle); lane 5, $_{CFP}[I–II]_{N\text{-intein}}$ + $_{C\text{-intein}}[III–IV^{TQ/YM}]_{YFP}$ (open triangle). Untagged β_{2a} is coexpressed in lanes 2–5. (*C*) Titration of $_{CFP}[I–II]_{N\text{-intein}}$ to $_{C\text{-intein}}[III–IV]_{YFP}$ transfection ratio (plus CFP-β_{2a}). (*D*) Confocal images showing CFP, YFP, and QD fluorescence in cells coexpressing $_{CFP}[I–II]_{N\text{-intein}}$ + $_{C\text{-intein}}[III–IV]_{YFP}$ ± β_{2a}. (Scale bar, 10 μm.) (*E*) Flow cytometry dot plot of YFP and QD fluorescence. (*F*) Quantification of QD_{655} signal. *P = 0.0000427 compared with −β using two-tailed unpaired t test. n = 5, 50,000 cells per experiment.

for effective targeting to the cell surface (27, 28) (Fig. 2*F*). To selectively label surface channels, nonpermeabilized HEK293 cells coexpressing $_{CFP}[I–II]_{N\text{-intein}}$ + $_{C\text{-intein}}[III–IV]_{YFP}$ ± β_{2a} were sequentially labeled with biotinylated α-bungarotoxin (BTX) and streptavidin-conjugated fluorescent quantum dots (QD_{655}). Channel surface expression was analyzed by confocal imaging (Fig. 2*D*) and flow cytometry (Fig. 2*E*). Quantification of fluorescence intensity signals indicated $Ca_V\beta$ increased surface expression of intein-spliced α_{1C} eightfold, similar to the magnitude of response seen with WT α_{1C} (Fig. 2*F*).

We next compared functional characteristics of currents reconstituted with intein-spliced α_{1C} subunits to those obtained with their full-length WT counterparts. LTCCs reconstituted with WT α_{1C} + β_{2a} generated robust whole-cell currents (Fig. 3*A*) that activated at a threshold potential of –30 mV and peaked at 0 mV (Fig. 3*B*). Moreover, WT channels were strongly and rapidly inhibited by 1 μM nifedipine, with complete loss of current observed for 5 μM and 10 μM nifedipine (Fig. 3 *A–C*). Intein-spliced WT α_{1C} channels reconstituted with $_{CFP}[I–II]_{N\text{-intein}}$ + $_{C\text{-intein}}[III–IV]_{YFP}$ + β_{2a} displayed virtually identical whole-cell currents and similar sensitivity to nifedipine as WT α_{1C} + β_{2a} (Fig. 3 *D–F* and Table S1). By contrast, intein-spliced DHP-resistant α_{1C} channels displayed currents that were relatively insensitive to nifedipine (Fig. 3 *G–I*). Expressing either $_{CFP}[I–II]_{N\text{-intein}}$ or $_{C\text{-intein}}[III–IV]_{YFP}$ separately did not yield either ionic or gating currents in HEK293 cells (Fig. S2). This contrasts with previous reports that expressing the I–II domain of $Ca_V1.1$ (α_{1S}) in skeletal myotubes results in measurable gating charge (24, 25). The difference could be due to either the distinct Ca_V1 isoforms or cell types involved.

Expression and Trafficking of Intein-Spliced α_{1C} in Adult Cardiomyocytes. Having validated the split-intein strategy in HEK293 cells, we next used this method to express LTCCs in adult cardiomyocytes. We chose adenoviral vectors because they readily infect adult cardiac myocytes and have a relatively fast onset of protein expression (<24 h). This is important because adult cardiac myocytes begin to dedifferentiate after 3–4 d in culture (2). We were unable to generate adenoviruses incorporating full-length α_{1C}, a common finding for many investigators in the field, that is attributable to the large insert size of α_{1C} and regulatory elements (~7.2 kb) being at the packaging capacity limit of adenoviral vectors. By contrast, both intein-tagged α_{1C} moieties were readily packaged into adenoviral vectors (Fig. 4*A*). We infected adult rat cultured cardiomyocytes with $_{CFP}[I–II]_{N\text{-intein}}$ and either $_{C\text{-intein}}[III–IV]_{YFP}$ or $_{C\text{-intein}}[III–IV^{TQ/YM}]_{YFP}$ and examined cells for protein expression 48 h after infection. The cardiomyocyte infection was highly efficient, with >90% of cells exhibiting robust CFP/YFP fluorescence, confirming expression of the intein-flanked α_{1C} moieties (Fig. 4*B*). Western blotting confirmed that the split-intein–tagged α_{1C} moieties were spliced to generate full-length protein in adult cardiomyocytes. Whole-cell lysates probed with anti-α_{1C} antibody detected both endogenous and intein-spliced α_{1C} (Fig. 4*B*). Intein-spliced α_{1C} was readily distinguishable from endogenous α_{1C} due to the presence of fluorescent protein tags that endowed them with a higher molecular weight. Intein-spliced α_{1C} expression level was titratable, with increasing protein expression observed at higher adenoviral doses (Fig. 4*B*).

To determine whether intein-spliced α_{1C} expressed in cardiomyocytes trafficked to the cell surface, we sequentially exposed nonpermeabilized infected cardiomyocytes to biotinylated BTX and streptavidin-conjugated QD_{655}. Cardiomyocytes coexpressing $_{CFP}[I–II]_{N\text{-intein}}$ and $_{C\text{-intein}}[III–IV]_{YFP}$ displayed robust red QD_{655} fluorescence staining of the surface sarcolemma (Fig. 4*C* and Fig. S3). As a negative control, uninfected myocytes showed negligible QD fluorescence (Fig. 4*C* and Fig. S3). Similarly, cardiomyocytes expressing only $_{CFP}[I–II]_{N\text{-intein}}$ displayed minimal QD_{655} surface staining, indicating this moiety alone does not traffic to the cell surface (Fig. S3).

In adult ventricular myocytes, the close proximity of LTCCs and RyR2s at dyadic junctions can be demonstrated using immunofluorescence analyses showing a high degree of colocalization between endogenous α_{1C} and RyR2 (Fig. 4*D*), in agreement with previous reports (5). To determine whether intein-spliced α_{1C} was properly targeted to dyads we performed coimmunofluorescence experiments using anti-GFP and anti-RyR antibodies (Fig. 4*D*). Much of the anti-GFP staining was observed in regularly spaced transverse patterns that occurred with a periodicity of 1.8 μm, consistent with the staining pattern of t tubules in cardiomyocytes (Fig. 4*D*). Most importantly, quantitative analyses indicated intein-spliced α_{1C} colocalized with RyR2s to the same extent as endogenous channels, as demonstrated by similar Pearson's correlation coefficient values (Fig. 4*E*). Similar values were obtained by quantifying this colocalization independently using Li's intensity correlation coefficient (29) (Fig. S4).

Beyond localization at dyads, a subset of LTCCs in ventricular myocytes associate with caveolin-3 and target to caveolae (7, 30). Consistent with this, endogenous LTCCs exhibit significant colocalization with caveolin-3 in adult cardiomyocytes (Fig. S4). It is unknown whether α_{1C} subunits that are targeted to dyads are molecularly distinct from those associated with caveolin-3. One possible mechanism for differential LTCC targeting in cardiomyocytes could be alternative splicing of α_{1C}. We discovered that intein-spliced α_{1C} also colocalizes with endogenous caveolin-3 in cardiomyocytes (Fig. S4), indicating molecularly identical α_{1C} subunits can target to both dyads and caveolae.

Overall, these results show that intein-tagged α_{1C} halves expressed in cardiomyocytes are efficiently spliced together to generate an intact α_{1C} that traffics to dyads and associates with caveolin-3 similar to the endogenous protein. Because no $Ca_V\beta$ was coexpressed in these experiments, the results suggest intein-spliced α_{1C} associates with endogenous $Ca_V\beta$ to traffic to the cell surface.

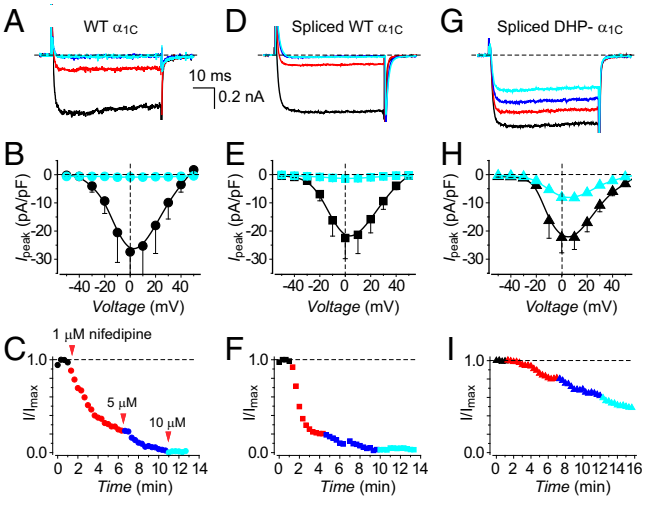

Fig. 3. Electrophysiological properties and DHP sensitivity of WT and split-intein–reconstituted LTCCs in HEK293 cells. (*A*) Exemplar Ba^{2+} currents from cells expressing full-length WT α_{1C} + β_{2a} in the absence (black trace) and presence of different nifedipine concentrations (1 μM, red; 5 μM, blue; 10 μM, cyan). (*B*) Population current-density versus voltage (*I–V*) relationship for cells expressing full-length WT α_{1C} + β_{2a} channels in the absence (black symbols) or presence (cyan symbols) of 10 μM nifedipine. $n = 7$ for each point. (*C*) Diary plots of nifedipine inhibition of full-length WT α_{1C} + β_{2a} channels. (*D–F*) Data for intein-spliced WT α_{1C} channels are in the same format as *A–C*. $n = 9$. (*G–I*) Data for intein-spliced DHP-resistant α_{1C} channels are in the same format as *A–C*. $n = 10$.

Functional Characterization of Intein-Spliced α_{1C} Subunits in Cardiomyocytes. We used whole-cell patch clamp to examine the functionality of intein-spliced α_{1C} subunits expressed in cardiomyocytes. Surprisingly, cardiomyocytes coexpressing $_{CFP}[I–II]_{N\text{-intein}}$ and either $_{C\text{-intein}}[III–IV]_{YFP}$ or $_{C\text{-intein}}[III–IV^{TQ/YM}]_{YFP}$ displayed only a marginal increase in Ba^{2+} current density compared with uninfected control myocytes (Fig. 5 *A–C*). One possible explanation for this result is that endogenous $Ca_V\beta$ subunits are rate-limiting for LTCC functional expression in heart. This interpretation would

PHYSIOLOGY

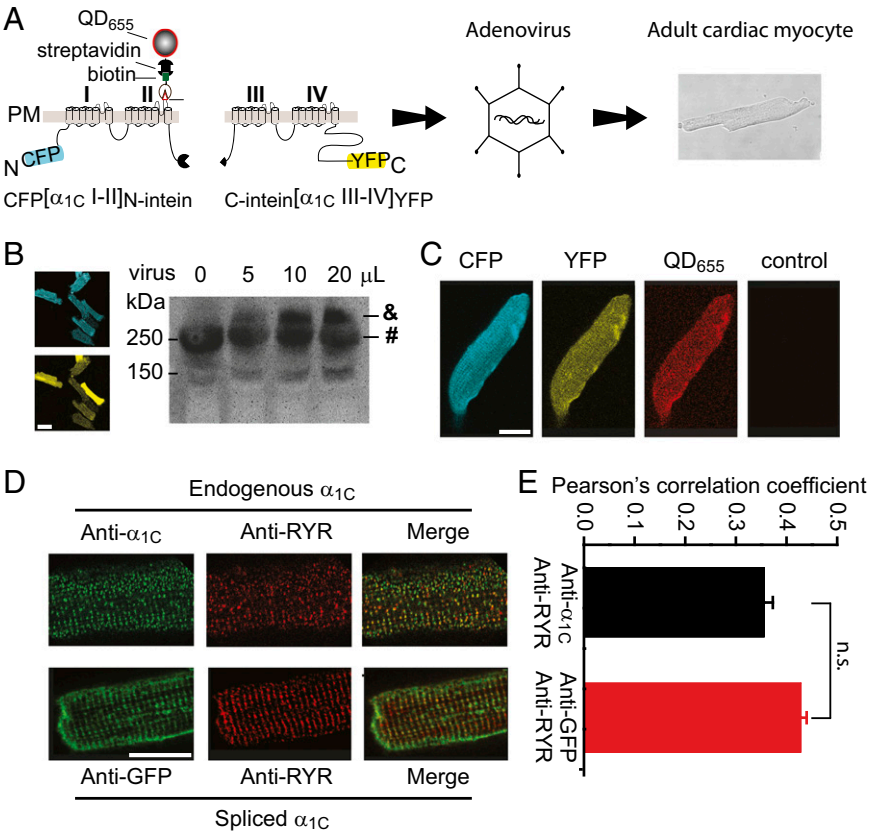

Fig. 4. Expression and subcellular targeting of intein-spliced α_{1C} in cardiac myocytes. (*A*) Schematic showing incorporation of split-intein–tagged α_{1C} moieties into adenovirus and infection of cardiomyocytes. (*B*, *Left*) Confocal images showing high efficiency expression of CFP- and YFP-tagged split-intein α_{1C} moieties in adult cardiomyocytes. (Scale bar, 50 μm.) (*B*, *Right*) Western blot (anti-α_{1C} antibody) detection of endogenous (#) and intein-spliced (&) α_{1C} subunits. (*C*) Confocal images of CFP, YFP, and QD_{655} fluorescence in a cardiomyocyte expressing intein-spliced α_{1C}. Control shows absence of QD_{655} staining in an uninfected cell. (Scale bar, 20 μm.) (*D*, *Upper*) Immunostaining of endogenous α_{1C} (anti-α_{1C}, green) and RyR (anti-RyR, red) in an uninfected cardiomyocyte. (*D*, *Lower*) Immunostaining of intein-spliced α_{1C} (anti-GFP, green) and endogenous RYR (anti-RyR, red). (Scale bar, 20 μm.) (*E*) Colocalization analyses.

be consistent with prior observations that overexpressing $Ca_V\beta$s alone in heart causes a several-fold increase in LTCC current density (11, 31). An alternate possibility was that the intein-spliced α_{1C} subunits were not functional despite making it to the cell surface (Fig. 4). To distinguish between the two possibilities we recorded currents in cardiomyocytes expressing either intein-spliced WT or DHP-resistant α_{1C} in the presence of 10 μM nifedipine (Fig. 5*D*). Under these conditions, cardiomyocytes expressing intein-spliced DHP– α_{1C} subunits expressed currents that were on average threefold larger than those expressing spliced WT α_{1C}, demonstrating that the expressed channels are functional (Fig. 5 *D* and *E*). We obtained a similarly large DHP-resistant current in cardiomyocytes coinfected with $_{CFP}$[I–II]$_{N\text{-intein}}$ and $_{C\text{-intein}}$[III–IV$^{TO/YM}$] expressed in a bicistronic adenovirus vector (Fig. S5). The bicistronic strategy can be used to overcome potential concerns that directly fusing fluorescent proteins to the α_{1C} fragments could disrupt aspects of their functions in some unanticipated way. Because DHP block of $Ca_V1.2$ is known to be voltage- and state-dependent, we examined whether we could achieve greater nifedipine separation of WT and DHP-resistant α_{1C} by using a –50 mV holding potential and 2 mM Ca^{2+} as charge carrier (Fig. S6). Under these conditions, WT $Ca_V1.2$ currents elicited by a ramp protocol were deeply inhibited by 10 μM nifedipine, whereas myocytes expressing intein-spliced DHP-resistant α_{1C} displayed a sevenfold larger remnant current (Fig. S6).

To determine the functional competence of intein-spliced α_{1C} to trigger CICR at dyads, we measured rhod-2–reported Ca^{2+} transients using line scan confocal microscopy (Fig. 6). Control uninfected cells responded to 1 Hz field stimulation with robust basal Ca^{2+} transients that were inhibited by 1 μM nifedipine (Fig. 6 *A* and *D*). In myocytes expressing either intein-spliced WT (Fig. 6*B*) or DHP– (Fig. 6*C*) α_{1C}, basal Ca^{2+} transients were marginally larger than observed in uninfected controls, consistent with a modest increase in the number of surface LTCCs (Fig. 6*D*). Ca^{2+} transients in cardiomyocytes expressing intein-spliced WT α_{1C} were inhibited by 1 μM nifedipine (90% inhibition), with most cells unresponsive to field stimulation (Fig. 6 *B* and *D*). By contrast, cardiomyocytes expressing spliced DHP-resistant α_{1C} were only modestly inhibited by 1 μM nifedipine (20% inhibition) and virtually all cells remained responsive to field stimulation. Exposure of cardiomyocytes expressing spliced WT α_{1C} to 5 μM nifedipine completely eliminated Ca^{2+} transients in response to field stimulation in eight out of eight cells (Fig. 6*E*), whereas six out of nine cells expressing spliced DHP-resistant α_{1C} remained responsive at this higher DHP concentration (Fig. 6*F*).

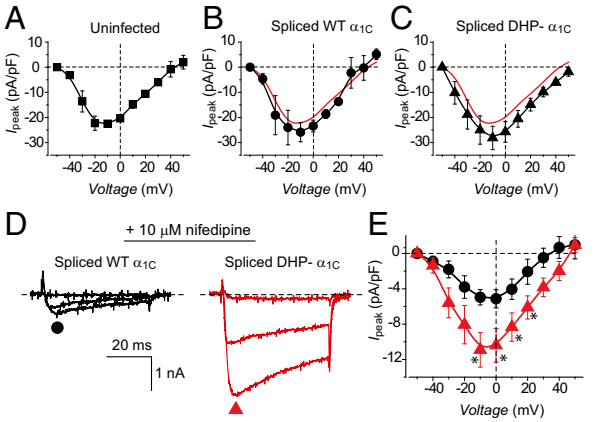

Fig. 5. Electrophysiological characterization of intein-spliced WT and DHP-resistant α_{1C} in cardiac myocytes. Population *J*–*V* relationships in (*A*) uninfected cardiomyocytes (control), (*B*) myocytes expressing intein-spliced WT α_{1C}, or (*C*) intein-spliced DHP– α_{1C}. (*D* and *E*) Exemplar current traces and population *J*–*V* curves from cardiomyocytes expressing either intein-spliced WT α_{1C} (black trace and symbols, $n = 9$) or DHP– α_{1C} (red trace and symbols, $n = 8$) channels in the presence of 10 μM nifedipine. $^*P = 0.018$ (–10 mV), $^*P = 0.0324$ (0 mV), $^*P = 0.048$ (10 mV), and $^*P = 0.04$ (20 mV) using two-tailed unpaired *t* test.

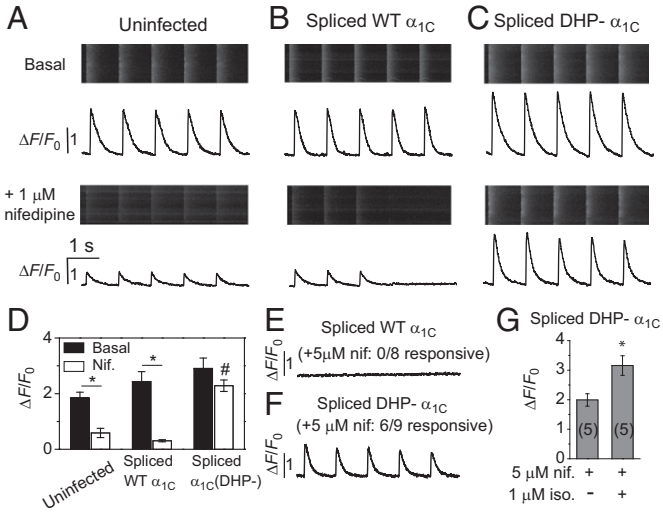

Fig. 6. Participation of intein-spliced WT and DHP– α_{1C} in CICR in cardiomyocytes. (*A*, *Upper*) The rhod-2-reported Ca^{2+} transients in an uninfected (UT) cardiomyocyte paced with 1 Hz field stimulation. (*A*, *Lower*) Ca^{2+} transients from UT myocyte in the presence of 1 μM nifedipine. (*B* and *C*) Ca^{2+} transients from cardiomyocytes expressing intein-spliced WT (α_{1C}) and DHP– α_{1C}, respectively. Same format as *A*. (*D*) Impact of 1 μM nifedipine on Ca^{2+} transient amplitudes. * $P = 0.0014$ (UT), * $P = 0.0003$ (α_{1C}), two-tailed unpaired *t* test. #, significantly different from control and intein-spliced WT α_{1C} +nifedipine using one-way ANOVA [$F(2, 12) = 47.48$, $P = 2E\text{-}6$] and Bonferroni pairwise comparisons, $n = 5$ cells. (*E*) CICR is abolished by 5 μM nifedipine in cardiomyocytes expressing intein-spliced WT α_{1C}. (*F*) Persistence of CICR in cardiomyocytes expressing intein-spliced DHP– α_{1C} in 5 μM nifedipine. (*G*) A total of 1 μM isoproterenol potentiates Ca^{2+} transients triggered by intein-spliced DHP– α_{1C}, *$P = 0.018$.

With the ability to completely isolate intein-spliced DHP-resistant α_{1C}-stimulated Ca^{2+} transients with 5 μM nifedipine, we examined whether this channel was permissive for sympathetic up-regulation of EC coupling under these experimental conditions. Exposure of cardiomyocytes expressing spliced DHP-resistant α_{1C} to 5 μM nifedipine + 1 μM isoproterenol resulted in Ca^{2+} transients with an elevated peak compared with those obtained with 5 μM nifedipine alone (Fig. 6*G*). The sympathetic elevation of Ca^{2+} transients under these conditions is likely due to a combination of PKA-dependent phosphorylation of $Ca_V1.2$, RYR2, and phospholamban (32).

Discussion

We have developed a unique method to readily manipulate tagged α_{1C} expression in isolated adult cardiomyocytes. The unique technology offers clear advantages over using heterologous expression systems to study the functional properties of cardiac LTCCs. Heterologous cells lack the unique cytoarchitecture of adult cardiomyocytes. Consequently, questions such as the mechanisms underlying differential LTCC targeting to dyads and caveolae, or their putative role in pathological cardiac hypertrophy, cannot be studied in noncardiomyocytes. It has also proven difficult to determine the mechanism of PKA-induced enhancement of LTCCs from heterologous expression experiments. Based on studies in HEK293 cells, it was suggested that phosphorylation of Ser1928 in α_{1C} and Ser478/Ser479 in β_{2a} was critical for PKA regulation of LTCCs (33, 34). However, the putative role of these phosphorylation sites in PKA regulation of LTCC was ruled out using α_{1C}[Ser1928Ala] mutant channels and truncated-β_2 knock-in mice (35, 36), as well as experiments in isolated adult cardiomyocytes (11, 37). More recent data using HEK293 point to an essential role for phosphorylation of Ser1700 and Thr1704 in PKA regulation of LTCCs (38). The importance of these residues has not been directly confirmed in cardiac myocytes. Overall, these discrepancies emphasize the importance of addressing questions pertaining to LTCC trafficking and functional regulation in the context of actual heart cells. A caveat is that the isoproterenol-induced increase in peak evoked Ca^{2+} release we measured was relatively modest and likely also includes contributions by PKA regulation of RYR and phospholamban. In part, the relatively modest response may be attributable to the use of rat cardiomyocytes in which PKA modulation of $Ca_V1.2$ is much less robust than in other species such as guinea pig (11). We are currently working to establish conditions for strong PKA modulation of spliced DHP-insensitive α_{1C} in guinea pig cardiomyocytes.

Knock-in mouse models are the gold standard for defining structure–function mechanisms of proteins in heart. The approach of manipulating α_{1C} expression with adenoviral vectors in isolated adult cardiomyocytes offers several advantages over knock-in mouse models. First, knock-in mice are costly and take up to 2 y to generate, making their routine use for in-depth structure–function studies requiring many different constructs impractical. By comparison, split-intein adenoviruses are more cost and time effective. Second, certain questions cannot be pursued in knock-in mice due to lethality of the knocked in gene. For example, knock-in mice featuring C-terminal truncations of α_{1C} unexpectedly display a marked decrease in L-type calcium current and die shortly after birth due to heart failure (39, 40). This precludes the use of knock-in mice to pursue relevant questions regarding the role of α_{1C} C terminus in LTCC trafficking and functional regulation in adult cardiomyocytes. Third, the adenoviral infection approach permits questions to be easily addressed in different species. This is important because the functional properties of murine cardiomyocytes differ in several critical ways from those of human, such as the action potential duration being considerably shorter in mice (41). There have been scattered reports of successful expression of LTCC α_{1C} subunits in adult cardiomyocytes (37, 42, 43). Previously, by additionally deleting the fiber gene from the standard adenoviral vector backbone (E1 and E3 deleted) and generating a complementing stable cell line, we were able to generate adenovirus containing full-length α_{1C} (37, 42). However, this system proved unstable and further attempts to generate new adenoviruses were unsuccessful. There has been one report using lentivirus to express α_{1C} subunits in adult rat cardiomyocytes (44). We generated lentiviruses expressing GFP-tagged α_{1C} truncated in the C terminus at residue 1905, which transduced HEK293 cells efficiently, expressing α_{1C}[1905]–GFP within 48 h. However, in our hands, the transduction efficiency of adult cardiomyocytes was low, and required several days for transgene expression, a problematic feature given the short half-life of rod-shaped cardiomyocytes in culture. Recently, a biolistic transfection method was adapted to express α_{1C} in adult rat ventricular myocytes (41). Compared with our approach, the biolistic method suffers from high toxicity (~10% viable cells) and relatively low transfection efficiency (~30% of surviving cells express transgene) (45).

Our unique application of split-intein technology engineers functional expression of a large protein with high efficiency in adult heart cells. Beyond LTCCs there are many other large cardiac proteins (e.g., voltage-gated sodium channel, ankyrin, spectrin, myosin, ryanodine receptor, and titin) whose structure–function properties, trafficking, and functional modulation in heart are of major interest, but currently only accessible using knock-in mice. The split-intein approach can be extended to explore the functional properties of many other large proteins in cardiomyocytes. Overall, the split-intein method expands the toolkit available, which includes high-capacity HSV-1 amplicon vectors (46), for manipulating expression of large genes in primary cardiac myocytes.

Materials and Methods

Generation of Plasmid and Adenoviral Vectors. GenBank IDs of cDNAs used are provided in Table S2. Detailed cloning strategies to generate expression plasmids are provided in *SI Materials and Methods*. PCR primer sequences used for cloning are provided in Table S3. Replication-deficient adenoviruses

were generated using the Clontech Adeno-X System 3. Viral expansion and purification was carried out as described (31).

Cell Culture and Transfection/Infection. HEK293 cells cultured on 60 mm dishes were transfected with the appropriate cDNA (6 μg each) and T-antigen (1 μg) using calcium phosphate precipitation. Adult rat cardiomyocytes were prepared as described (31, 47) and cultured in medium supplemented with 0.5 μM cytochalasin D to preserve cell morphology (48). Cells were infected with 5–15 μL of viral stock in a final volume of 1–2 mL.

Quantum Dot Detection of Cell Surface BBS-Tagged LTCCs. Surface LTCCs in HEK293 cells or cardiomyocytes were labeled with quantum-dots as described (21), and assayed by flow cytometry using a BD LSR II Cell Analyzer (BD Biosciences). Flow cytometry data were analyzed using FloJo Software (21).

Intracellular Calcium Transient Measurements. Primary myocytes in culture were loaded with the calcium-sensing dye rhod2–AM. Evoked intracellular calcium transients were measured as described in *SI Materials and Methods*.

Image Processing and Analysis. Confocal images were analyzed using ImageJ software and background subtracted. Colocalization of CFP/YFP, α_{1C}/RyR, and α_{1C}/caveolin-3 was carried out using the ImageJ JaCoP plugin. Colocalization in two channels was quantified using Pearson's and Li's colocalization coefficient algorithms in JaCoP (29).

Electrophysiology. Whole-cell recordings were conducted on HEK293 cells 48 h posttransfection using an EPC-8 patch clamp amplifier (HEKA Electronics) controlled by PULSE software as previously described (21, 28). Whole-cell recordings of rat ventricular myocytes were performed as described previously (31).

Analysis and Statistics. Data were plotted and statistical analyses performed in Origin software using built-in functions. Significant differences between means ($P < 0.05$, $P < 0.01$) were determined using Student *t* test for comparison between two groups, or one-way ANOVA followed by Bonferroni post hoc analyses for comparisons involving more than two groups. Data are represented as means ± SEM.

ACKNOWLEDGMENTS. We thank Prof. Tom W. Muir (Princeton University) for the generous gift of the plasmids containing *N. punctiforme* DnaE split-intein cDNA and Ming Chen for technical support. This work was supported by Grant R01 HL 069911 from the National Institutes of Health (to H.M.C.). H.M.C. is an Established Investigator of the American Heart Association.

1. Bers D (2001) *Excitation-Contraction Coupling and Cardiac Contractile Force* (Kluwer Academic Publishers, Dordrecht, the Netherlands), 2nd Ed, p 427.
2. Louch WE, Sheehan KA, Wolska BM (2011) Methods in cardiomyocyte isolation, culture, and gene transfer. *J Mol Cell Cardiol* 51(3):288–298.
3. Vinge LE, Raake PW, Koch WJ (2008) Gene therapy in heart failure. *Circ Res* 102(12): 1458–1470.
4. Bers DM (2002) Cardiac excitation-contraction coupling. *Nature* 415(6868):198–205.
5. Scriven DR, Dan P, Moore ED (2000) Distribution of proteins implicated in excitation-contraction coupling in rat ventricular myocytes. *Biophys J* 79(5):2682–2691.
6. Fabiato A (1983) Calcium-induced release of calcium from the cardiac sarcoplasmic reticulum. *Am J Physiol* 245(1):C1–C14.
7. Balijepalli RC, Foell JD, Hall DD, Hell JW, Kamp TJ (2006) Localization of cardiac L-type Ca(2+) channels to a caveolar macromolecular signaling complex is required for beta (2)-adrenergic regulation. *Proc Natl Acad Sci USA* 103(19):7500–7505.
8. Makarewich CA, et al. (2012) A caveolae-targeted L-type Ca^{2}+ channel antagonist inhibits hypertrophic signaling without reducing cardiac contractility. *Circ Res* 110(5): 669–674.
9. Shaw RM, Colecraft HM (2013) L-type calcium channel targeting and local signalling in cardiac myocytes. *Cardiovasc Res* 98(2):177–186.
10. Reuter H, Scholz H (1977) The regulation of the calcium conductance of cardiac muscle by adrenaline. *J Physiol* 264(1):49–62.
11. Miriyala J, Nguyen T, Yue DT, Colecraft HM (2008) Role of CaVbeta subunits, and lack of functional reserve, in protein kinase A modulation of cardiac CaV1.2 channels. *Circ Res* 102(7):e54–e64.
12. Zong X, et al. (1995) On the regulation of the expressed L-type calcium channel by cAMP-dependent phosphorylation. *Pflugers Arch* 430(3):340–347.
13. Catterall WA (2010) Signaling complexes of voltage-gated sodium and calcium channels. *Neurosci Lett* 486(2):107–116.
14. Perler FB, et al. (1994) Protein splicing elements: Inteins and exteins—a definition of terms and recommended nomenclature. *Nucleic Acids Res* 22(7):1125–1127.
15. Lockless SW, Muir TW (2009) Traceless protein splicing utilizing evolved split inteins. *Proc Natl Acad Sci USA* 106(27):10999–11004.
16. Muralidharan V, Muir TW (2006) Protein ligation: An enabling technology for the biophysical analysis of proteins. *Nat Methods* 3(6):429–438.
17. Iwai H, Züger S, Jin J, Tam PH (2006) Highly efficient protein trans-splicing by a naturally split DnaE intein from Nostoc punctiforme. *FEBS Lett* 580(7):1853–1858.
18. Zettler J, Schütz V, Mootz HD (2009) The naturally split Npu DnaE intein exhibits an extraordinarily high rate in the protein trans-splicing reaction. *FEBS Lett* 583(5): 909–914.
19. Catterall WA (2000) Structure and regulation of voltage-gated Ca2+ channels. *Annu Rev Cell Dev Biol* 16:521–555.
20. Sekine-Aizawa Y, Huganir RL (2004) Imaging of receptor trafficking by using alpha-bungarotoxin-binding-site-tagged receptors. *Proc Natl Acad Sci USA* 101(49):17114–17119.
21. Yang T, Xu X, Kernan T, Wu V, Colecraft HM (2010) Rem, a member of the RGK GTPases, inhibits recombinant CaV1.2 channels using multiple mechanisms that require distinct conformations of the GTPase. *J Physiol* 588(Pt 10):1665–1681.
22. He M, Bodi I, Mikala G, Schwartz A (1997) Motif III S5 of L-type calcium channels is involved in the dihydropyridine binding site. A combined radioligand binding and electrophysiological study. *J Biol Chem* 272(5):2629–2633.
23. Mitterdorfer J, et al. (1996) Two amino acid residues in the IIIS5 segment of L-type calcium channels differentially contribute to 1,4-dihydropyridine sensitivity. *J Biol Chem* 271(48):30330–30335.
24. Ahern CA, et al. (2001) Intramembrane charge movements and excitation- contraction coupling expressed by two-domain fragments of the Ca2+ channel. *Proc Natl Acad Sci USA* 98(12):6935–6940.
25. Flucher BE, Weiss RG, Grabner M (2002) Cooperation of two-domain Ca(2+) channel fragments in triad targeting and restoration of excitation-contraction coupling in skeletal muscle. *Proc Natl Acad Sci USA* 99(15):10167–10172.
26. Raghib A, et al. (2001) Dominant-negative synthesis suppression of voltage-gated calcium channel Cav2.2 induced by truncated constructs. *J Neurosci* 21(21):8495–8504.
27. Buraei Z, Yang J (2010) The ß subunit of voltage-gated Ca2+ channels. *Physiol Rev* 90(4):1461–1506.
28. Fang K, Colecraft HM (2011) Mechanism of auxiliary β-subunit-mediated membrane targeting of L-type (Ca(V)1.2) channels. *J Physiol* 589(Pt 18):4437–4455.
29. Bolte S, Cordelières FP (2006) A guided tour into subcellular colocalization analysis in light microscopy. *J Microsc* 224(Pt 3):213–232.
30. Nichols CB, et al. (2010) Sympathetic stimulation of adult cardiomyocytes requires association of AKAP5 with a subpopulation of L-type calcium channels. *Circ Res* 107(6):747–756.
31. Colecraft HM, et al. (2002) Novel functional properties of Ca(2+) channel beta subunits revealed by their expression in adult rat heart cells. *J Physiol* 541(Pt 2):435–452.
32. Luo W, et al. (1998) Transgenic approaches to define the functional role of dual site phospholamban phosphorylation. *J Biol Chem* 273(8):4734–4739.
33. Bünemann M, Gerhardstein BL, Gao T, Hosey MM (1999) Functional regulation of L-type calcium channels via protein kinase A-mediated phosphorylation of the beta(2) subunit. *J Biol Chem* 274(48):33851–33854.
34. Gao T, et al. (1997) cAMP-dependent regulation of cardiac L-type Ca2+ channels requires membrane targeting of PKA and phosphorylation of channel subunits. *Neuron* 19(1):185–196.
35. Brandmayr J, et al. (2012) Deletion of the C-terminal phosphorylation sites in the cardiac β-subunit does not affect the basic β-adrenergic response of the heart and the Ca(v)1.2 channel. *J Biol Chem* 287(27):22584–22592.
36. Lemke T, et al. (2008) Unchanged beta-adrenergic stimulation of cardiac L-type calcium channels in Ca v 1.2 phosphorylation site S1928A mutant mice. *J Biol Chem* 283(50):34738–34744.
37. Ganesan AN, Maack C, Johns DC, Sidor A, O'Rourke B (2006) Beta-adrenergic stimulation of L-type Ca2+ channels in cardiac myocytes requires the distal carboxyl terminus of alpha1C but not serine 1928. *Circ Res* 98(2):e11–e18.
38. Fuller MD, Emrick MA, Sadilek M, Scheuer T, Catterall WA (2010) Molecular mechanism of calcium channel regulation in the fight-or-flight response. *Sci Signal* 3(141):ra70.
39. Fu Y, et al. (2011) Deletion of the distal C terminus of CaV1.2 channels leads to loss of beta-adrenergic regulation and heart failure in vivo. *J Biol Chem* 286(14):12617–12626.
40. Domes K, et al. (2011) Truncation of murine CaV1.2 at Asp-1904 results in heart failure after birth. *J Biol Chem* 286(39):33863–33871.
41. Nerbonne JM, Kass RS (2005) Molecular physiology of cardiac repolarization. *Physiol Rev* 85(4):1205–1253.
42. Ganesan AN, et al. (2005) Reverse engineering the L-type Ca2+ channel alpha1c subunit in adult cardiac myocytes using novel adenoviral vectors. *Biochem Biophys Res Commun* 329(2):749–754.
43. Walsh KB, Zhang J, Fuseler JW, Hilliard N, Hockerman GH (2007) Adenoviral-mediated expression of dihydropyridine-insensitive L-type calcium channels in cardiac ventricular myocytes and fibroblasts. *Eur J Pharmacol* 565(1-3):7–16.
44. Thiel WH, et al. (2008) Proarrhythmic defects in Timothy syndrome require calmodulin kinase II. *Circulation* 118(22):2225–2234.
45. Dou Y, et al. (2010) Normal targeting of a tagged Kv1.5 channel acutely transfected into fresh adult cardiac myocytes by a biolistic method. *Am J Physiol Cell Physiol* 298(6):C1343–C1352.
46. Ferrera R, et al. (2005) Efficient and non-toxic gene transfer to cardiomyocytes using novel generation amplicon vectors derived from HSV-1. *J Mol Cell Cardiol* 38(1): 219–223.
47. Xu X, Colecraft HM (2009) Primary culture of adult rat heart myocytes. *J Vis Exp*, 10.3791/1308.
48. Tian Q, et al. (2012) Functional and morphological preservation of adult ventricular myocytes in culture by sub-micromolar cytochalasin D supplement. *J Mol Cell Cardiol* 52(1):113–124.

Supporting Information

Subramanyam et al. 10.1073/pnas.1308161110

SI Materials and Methods

Molecular Biology: Cloning Strategies for All Expression Plasmids Used. *Generation of intein-flanked α_{1C} constructs in pcDNA3.1.* Plasmids containing the DnaE split inteins (DnaE-n and DnaE-c) were a generous gift from Tom W. Muir (Princeton University, Princeton, NJ). The split inteins were originally cloned from the cyanobacteria *Nostoc punctiforme* PCC-73102 (http://tools.neb.com/inbase/) (1–3). Amino acid sequence of DnaE-n and DnaE-c are shown in Fig. S1.

To create $_{CFP}$[I–II]$_{N\text{-intein}}$ we first used overlap extension PCR to fuse a 450 bp fragment (Table S3, primers 1 and 2,) of α_{1C}[bungarotoxin-binding site, BBS]–YFP[21] (stretching from a unique EcoRI site to residue Pro871 in the middle of the II–III loop) upstream of a 342 bp fragment (primers 3 and 4) comprising the *N. punctiforme* DnaE-n sequence and a unique C-terminal XbaI site. The resulting 760 bp final fragment (containing 435 and 325 bp from α_{1C} and DnaE-n plasmids, respectively) was cloned into α_{1C}[BBS]–YFP in the plasmid construct pcDNA3 using EcoRI and XbaI to yield [I–II]$_{N\text{-intein}}$. A second overlap extension PCR was used to fuse a 748 bp fragment (primers 5 and 6) of CFP with a unique N terminus HindIII site upstream of the first 449 bp of α_{1C}[I–II]$_{N\text{-intein}}$ (primers 7 and 8) including a unique C terminus ClaI site. The resulting 1,167 bp fragment (containing 734 and 433 bp from CFP and α_{1C}[I–II]$_{N\text{-intein}}$, respectively) was cloned into α_{1C}[I–II]$_{N\text{-intein}}$ in pcDNA3 using HindIII and ClaI sites, yielding $_{CFP}$[I–II]$_{N\text{-intein}}$ in pcDNA3.

To create $_{C\text{-intein}}$[III–IV]$_{YFP}$, we used overlap extension PCR to fuse a 141 bp fragment (primers 9 and 10) comprising the *N. punctiforme* DnaE-c cDNA sequence with a unique N-terminal KpnI upstream of a 947 bp fragment (primers 11 and 12) from α_{1C}[BBS]–YFP starting at Glu873 in the II–III loop to a unique C-terminal Tth111I site. The resulting 1,062 bp fragment (containing 130 and 932 bp from DnaE-c and α_{1C}, respectively) was cloned into α_{1C}[BBS]–YFP in pcDNA3 using KpnI and Tth111I sites yielding $_{C\text{-intein}}$[III–IV]$_{YFP}$ in pcDNA3. We used overlap extension PCR (primers 13–16) to introduce T1066Y and Q1070M mutations into $_{C\text{-intein}}$[III–IV]$_{YFP}$ to generate $_{C\text{-intein}}$[III–IV$^{TQ/YM}$]$_{YFP}$.

Generation of intein-flanked α_{1C} constructs in adenoviral vector plasmids. Sequences for $_{CFP}$[I–II]$_{N\text{-intein}}$ (primers 17 and 18), $_{C\text{-intein}}$[III–IV]$_{YFP}$ (primers 19 and 20), and $_{C\text{-intein}}$[III–IV$^{TQ/YM}$]$_{YFP}$ (primers 19 and 20) were amplified by PCR and cloned into pShuttle-CMV vector (Stratagene) using KpnI/XhoI sites. Shuttle vectors were linearized with PmeI and electroporated into BJ5183-AD-1 electrocompetent cells (pretransformed with the pAdEasy-1 viral plasmid; Stratagene). Transformants with successful recombination were confirmed by restriction digestion using PacI. Positive recombinants were amplified using recombination-deficient XL-10-Gold bacterial strain. Purified recombinant adenoviral plasmid DNA is then digested with PacI to expose the inverted terminal repeats (ITRs) before transfection into AD-293 cells using calcium phosphate DNA precipitation.

To generate split-intein α_{1C} III–IV domain fragments that did not contain fused YFP, we PCR-amplified $_{C\text{-intein}}$[III–IV] and $_{C\text{-intein}}$[III–IV$^{TQ/YM}$] (primers 21 and 22) and included a stop codon after the coding sequence. The PCR products were cloned into pAdEasy dsRed Express using In-Fusion reaction according to the manufacturer's instructions (Clontech). The completed In-Fusion reaction was used to transform competent Stellar *Escherichia coli*, and recombinant clones identified by restriction digestion with XhoI. Plasmid DNA from positive clones were digested with PacI to expose viral ITRs and transfected into HEK293 cells to generate replication-deficient adenoviruses.

Generation of adenoviruses. HEK cells cultured in 60 mm diameter dishes at 70–80% confluency were transfected with *Pac*I-digested linearized adenoviral DNA. Transfected plates were monitored for cytopathic effects (CPEs) and adenoviral plaques. Cells were harvested and subjected to three consecutive freeze-thaw cycles, followed by centrifugation (3,900 × *g*) to remove cellular debris. The supernatant (2 mL) was used to infect a 10 cm dish of 90% confluent HEK293 cells. Following observation of CPEs after 2–3 d, cell supernatants were used to reinfect a new plate of HEK293 cells. Viral expansion and purification was carried out as previously described (4). Briefly, confluent HEK293 cells grown on 15 cm culture dishes were infected with viral supernatant (1 mL) obtained as described above. We used 8–10 plates per preparation. After 48 h, cells from all of the plates were harvested, pelleted by centrifugation, and resuspended in 8 mL of buffer containing (in mM) Tris·HCl 20, $CaCl_2$ 1, and $MgCl_2$ 1 (pH 8.0). Cells were lysed by four consecutive freeze-thaw cycles and cellular debris pelleted by centrifugation. The virus-laden supernatant was purified on a cesium chloride (CsCl) discontinuous gradient by layering three densities of CsCl (1.25, 1.33, and 1.45 g/mL). After centrifugation (50,000 rpm; SW41Ti Rotor, Beckman-Coulter Optima L-100K ultracentrifuge; 1 h, 4 °C), a band of virus at the interface between the 1.33 and 1.45 g/mL layers was removed and dialyzed against PBS (12 h, 4 °C).

Transfection of HEK293 Cells Using Calcium Phosphate–DNA Precipitation. Briefly, plasmid DNA was mixed with 62 μL of 2.5M $CaCl_2$ and sterile deionized water (to a final volume of 500 μL). The mixture was added dropwise, with constant tapping to 500 μL of 2× Hepes buffered saline (HBS) (in mM: Hepes 50, NaCl 280, Na_2HPO4 1.5, pH 7.09). The resulting DNA–calcium phosphate mixture was allowed to sit for 20 min, followed by dropwise addition to confluent HEK cells. Cells were washed with serum-free DMEM after 8 h and maintained in supplemented DMEM.

Culture of Primary Adult Rat Ventricular Myocytes. Primary cultures of adult rat heart ventricular cells were prepared as previously described (4, 5). Adult male Sprague–Dawley rats were killed with an overdose of halothane in accordance with the guidelines of Columbia University Animal Care and Use Committee. Hearts were excised and ventricular myocytes isolated by enzymatic digestion with 1.7 mg Liberase–TM enzyme mix (Roche) using a Langendorff perfusion apparatus. Healthy rod-shaped myocytes were cultured in Medium 199 (Life Technologies) supplemented with (in mM) carnitine (5), creatine (5), taurine (5) penicillin-streptomycin-glutamine (0.5%, Life technologies), and 5% (vol/vol) FBS (Life Technologies) to promote attachment to dishes. After 5 h, the culture medium was switched to Medium 199 with 1% (vol/vol) serum, but otherwise supplemented as described above. Cultures were maintained in humidified incubators at 37 °C and 5% CO_2.

Quantum Dot Labeling of Cell Surface BBS-tagged L-Type Calcium Channels. Transfected HEK293 cells or fixed cardiomyocytes were used for this assay. At 48 h posttransfection or postinfection, cells on 35 mm MatTek dishes (MatTek Corporation) were gently washed with PBS with Ca^{2+} and Mg^{2+} (in mM: 0.9 $CaCl_2$, 0.49 $MgCl_2$, pH 7.4) and then incubated for 30 min in blocking medium [DMEM with 3% (wt/vol) BSA]. Cells were then incubated with 1 μM biotinylated α-bungarotoxin (BTX; Life Technologies) in DMEM/3% BSA at room temperature (RT) for 1 h followed by washing twice with DMEM/3% BSA to

remove unbound biotinylated BTX. Cells were then incubated with 10 nM streptavidin-conjugated quantum dot $(QD)_{655}$ (Life Technologies) for 1 h at 4 °C in the dark.

Immunofluorescence Staining. Primary cultured myocytes infected with viruses encoding appropriate constructs were used in this assay. At 48 h postinfection, myocytes were fixed with a 4% (wt/vol) solution of paraformadehyde in PBS for 20 min at RT. Cells were washed twice with PBS for 10 min each, followed by incubation in PBS with 0.1 M glycine (10 min, RT) to block free aldehyde groups. Fixed cells were permeabilized using PBS supplemented with 0.2% Triton X-100 (20 min). Nonspecific binding was blocked by incubation of the cells in PBS with 0.1% Triton, 3% (vol/vol) normal goat serum (NGS), and 1% (wt/vol) BSA (1 h, RT). Cells were subsequently incubated with primary antibodies in PBS with 0.1% Triton, 1% NGS, and 1% BSA (4 h, RT). Cells were washed three times for 10 min each with PBS with 0.1% Triton followed by staining with fluorescent secondary antibodies (1 h, RT). Antibody dilutions were prepared in PBS with 0.1% Triton, 1% NGS, and 1%BSA. The cells were then washed with PBS/0.1% Triton. Cells were imaged immediately in the same buffer.

Confocal Laser Scanning Microscopy: Laser Lines and Detector Settings. The following laser lines and detector settings were used: CFP, 405 nm diode laser, 465–502 nm detection; Alexa 488, 488 nm Ar ion, 500–540 nm detection; YFP, 514nm Ar ion, 520–560 nm detection; Alexa 555, 543 nm HeNe, 550–600 nm detection; and QD_{655}, 405 nm diode laser, 620–700 nm detection. Laser power was set at 30% and detector gain at 550–700 V to reduce noise and prevent saturation of image pixels. Pinhole size was set at 1 Airy unit.

Intracellular Calcium Transient Measurements. Primary myocytes in culture were loaded with rhod2–AM (5 μM with 0.05% Pluronic F127 detergent) in Tyrode solution (containing in mM: NaCl 138, KCl 4, CaCl2 2, MgCl2 1, NaH_2PO_4 0.33, and Hepes 10) for 20 min at RT. Cells were then washed and maintained in Tyrode. The Leica SP2 microscope equipped with a 63×, oil immersion, N.A. 1.4 objective was used for confocal linescan imaging. The electronic zoom was adjusted to fit the cells, and the scan field was rotated to be along the long axis of the cells. Static bright-field and fluorescent images were taken before measuring intracellular Ca^{2+} release. Rhod-2 was excited at 543 nm and emission detected between 550–600 nm. Cells were paced at 1 Hz using a Myopacer EP (Ion Optix). Confocal linescan frequency was set at 400 Hz and cells were scanned for 20 s.

Electrophysiology. Whole-cell recordings were conducted at RT on transfected HEK293 cells 48 h posttransfection using an EPC-8 patch clamp amplifier (HEKA Electronics) controlled by PULSE software (HEKA). Micropipettes were prepared from 1.5 mm thin-walled glass (World Precision Instruments) using a P97 microelectrode puller (Sutter Instruments). The internal solution contained (in mM) cesium methanesulfonate (135), cesium chloride (5), EGTA (5), $MgCl_2$ (1), MgATP (4, added fresh), and Hepes (10, pH 7.4). When filled with internal solution, the resistance of the pipette was typically 1.7–2.5 MΩ. External solution contained (in mM) tetraethylammonium-methanesulfonate (140), $BaCl_2$ (5), and Hepes (10, pH 7.4). There was no electronic series resistance compensation. Currents were sampled at 25 KHz and filtered at 10 KHz. Traces were acquired at a repetition interval of 6 s. Leak and capacitive currents were subtracted using a P/8 protocol.

For whole-cell recordings of cultured rat ventricular myocytes, microelectrodes typically had a resistance of 1–2 MΩ when filled with an internal solution containing (in mM) cesium-methanesulfonate (150), EGTA (10), CsCl (5), $MgCl_2$ (1), MgATP (4, added fresh), and Hepes (10). For formation of gigaohm seals and initial break-in to the whole-cell configuration, cells were perfused with normal tyrode solution containing (in mM) NaCl (138), KCl (4), $CaCl_2$ (2), $MgCl_2$ (1), NaH_2PO4 (0.33), and Hepes (10, pH 7.4). Following successful break-in, the perfusing medium was switched to an external recording solution containing (mM) *N*-methy-D-glucamine-aspartate (155), 4-aminopyridine (10), $MgCl_2$ (1), $BaCl_2$ (5), and Hepes (10, pH 7.4 adjusted with *N*-methyl-D-glucamine). Signals were filtered at 2 KHz and sampled at 25 KHz. Data traces were acquired at a repetition interval of 45 s. Leak and capacitive currents were subtracted using a P/8 protocol.

Western Blotting. HEK293 cells and adult rat ventricular myocytes were harvested in lysis buffer containing (in mM) Tris (20, pH 7.4), EDTA (1), NaCl (150), 1% (wt/vol) SDS, 0.1% Triton X-100, and supplemented with protease inhibitor mixture (10 μL/mL, Sigma-Aldrich). Cells were lysed with three pulses of sonication for 10 s each. Total protein concentration in cell lysates was determined using the bis-cinchonic acid protein estimation kit (Pierce Technologies). Lysates were boiled (95 °C, 10 min) after addition of sample buffer [50 mM Tris, 10% (vol/vol) glycerol, 2% SDS, 100 mM DTT, and 0.2 mg/mL bromophenol blue]. Proteins were resolved on a 4–12% Bis·Tris gradient precast gel (Life Technologies) in Mops-SDS running buffer (Life Technologies) at 200 V constant for 1 h. We loaded 15 μL of the Precision Plus All Blue molecular weight standard (10–250 kDa, BioRad) alongside the samples. Protein bands were transferred by tank transfer onto a nitrocellulose membrane (2.5 h, 4 °C, 30 V constant) in transfer buffer (25 mM Tris pH 8.3, 192 mM glycine, 15% (vol/vol) methanol, and 0.1% SDS). The membranes were blocked with a solution of 5% nonfat milk (BioRad) in tris-buffered saline-tween (TBS-T) (25 mM Tris pH 7.4, 150 mM NaCl, and 0.1% Tween-20) for 1 h at RT and then incubated overnight at 4 °C with primary antibodies in blocking solution. The blots were washed with TBS-T three times for 10 min each and then incubated with secondary horseradish peroxidase-conjugated antibody for 1 h at RT. After washing in TBS-T, the blots were developed with a chemiluminiscent detection kit (Pierce Technologies) and then visualized on a gel imager.

1. Perler FB, et al. (1994) Protein splicing elements: Inteins and exteins—a definition of terms and recommended nomenclature. *Nucleic Acids Res* 22(7):1125–1127.
2. Iwai H, Züger S, Jin J, Tam PH (2006) Highly efficient protein trans-splicing by a naturally split DnaE intein from Nostoc punctiforme. *FEBS Lett* 580(7):1853–1858.
3. Zettler J, Schütz V, Mootz HD (2009) The naturally split Npu DnaE intein exhibits an extraordinarily high rate in the protein trans-splicing reaction. *FEBS Lett* 583(5): 909–914.
4. Colecraft HM, et al. (2002) Novel functional properties of Ca(2+) channel beta subunits revealed by their expression in adult rat heart cells. *J Physiol* 541(Pt 2):435–452.
5. Xu X, Colecraft HM (2009) Primary culture of adult rat heart myocytes. *J Vis Exp*, 10.3791/1308.

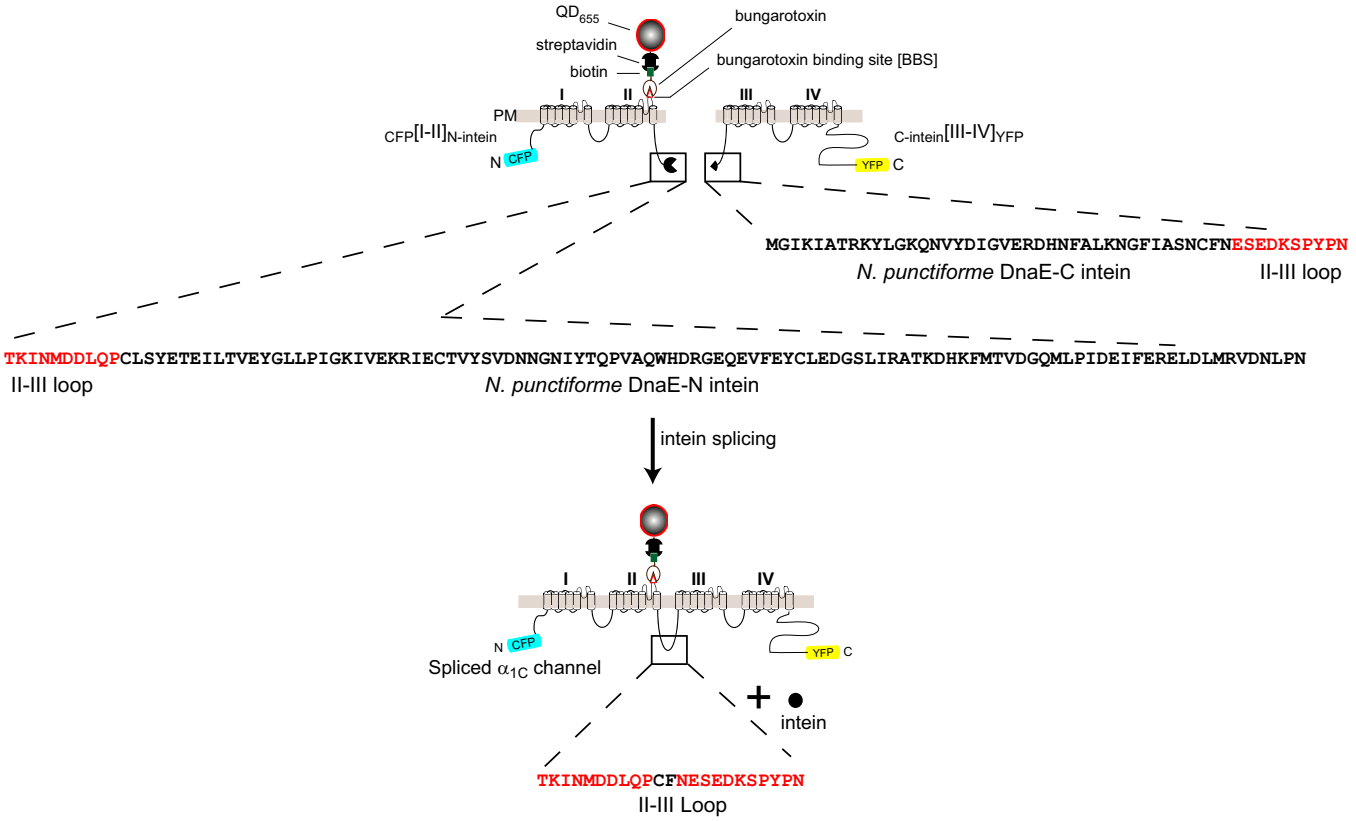

Fig. S1. Design of the intein-flanked α_{1C} moieties. (*Upper*) Depiction of the CFP- and YFP-tagged α_{1C} halves with location of the extracellular BBS tag and precise intein splice site within the II–III loop. Intein amino acid sequence (black) and II–III loop at splice site (red) is given. (*Lower*) Postsplicing inteins facilitate joining of α_{1C} halves, leaving three intein residues—C,F, and N—in the spliced product. Taking advantage of an α_{1C} asparagine residue at the split site, construct design ensures only two foreign residues are left behind: C and F.

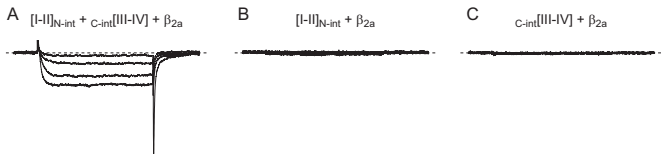

Fig. S2. (*A*) Exemplar whole-cell current traces and gating charge movement in cells expressing intein-spliced α_{1C}. (*B* and *C*) Cells expressing either $_{CFP}[I–II]_{N\text{-intein}}$ or $_{C\text{-intein}}[III–IV]_{YFP}$ separately do not exhibit either currents or gating charge movement. $n = 3$ for each condition.

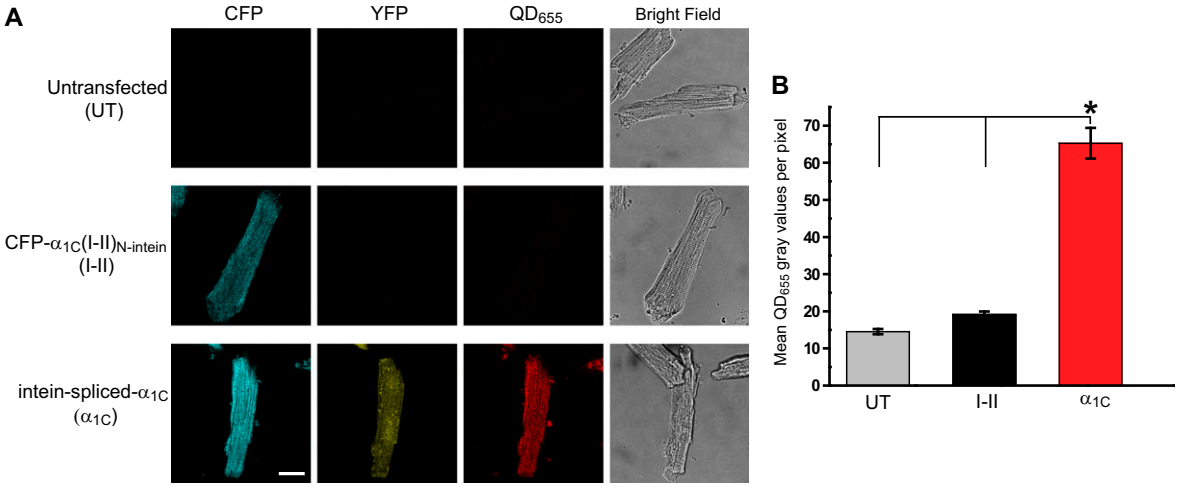

Fig. S3. Surface trafficking of intein-spliced α_{1C} subunits in cardiomyocytes. (*A*) Confocal images of myocytes depicting bright-field images, CFP/YFP fluorescence, and QD_{655} surface staining of extracellular BBS tag present in intein-spliced α_{1C} channel moieties. Uninfected control myocytes (*Top*, UT) and myocytes expressing either $_{CFP}[\alpha_{1C}$ I–II$]_{N\text{-intein}}$ (*Middle*, I–II) or intein-spliced α_{1C} (*Bottom*, α_{1C}) are shown. QD_{655} signal is negligible in uninfected myocytes and those expressing only the N-terminal moiety but is very robust in myocytes expressing intein-spliced α_{1C}. (Scale bar, 20 μm.) (*B*) Quantitation of QD_{655} signal shown in *A*. Mean gray values per pixel were calculated for each image acquired in QD_{655} channel for a population of 15 cells from each condition. Myocytes expressing intein-spliced α_{1C} showed significantly higher QD_{655} signal. Error bars, SEM; * significantly different from UT and I–II using one-way ANOVA [$F(2, 50) = 108.9$, $P = 1.02E\text{-}16$] and Bonferonni pairwise comparisons. $n = 15$ cells for each condition.

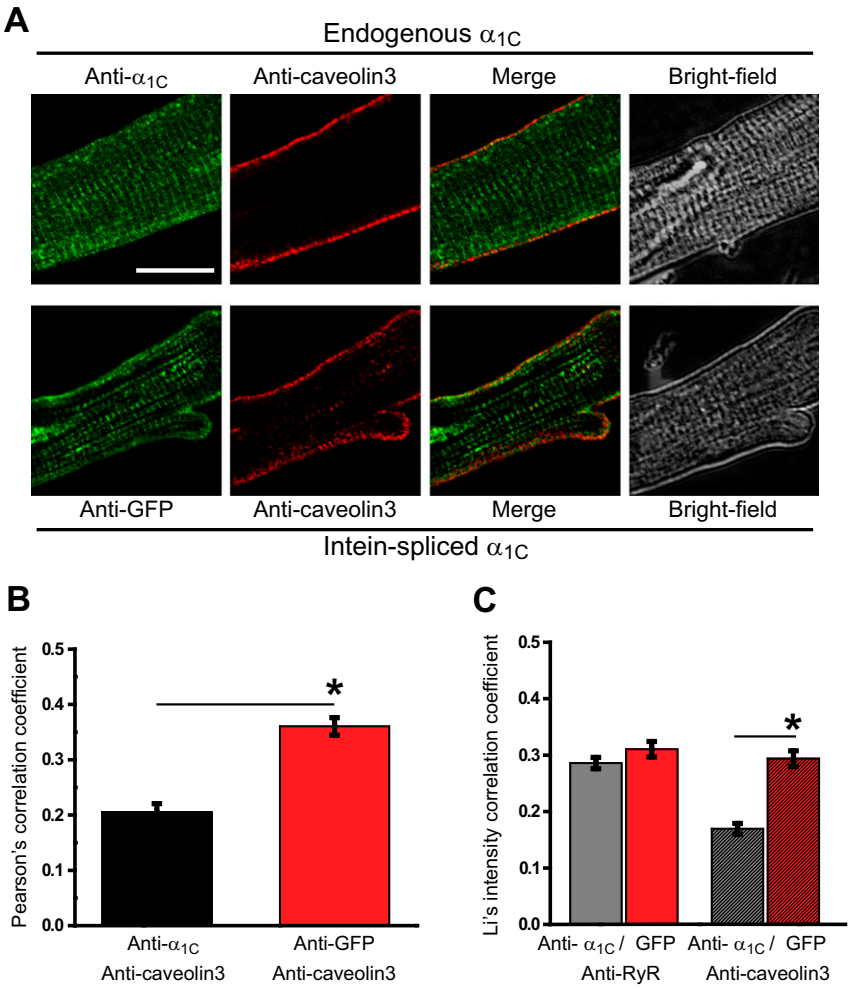

Fig. S4. Colocalization of intein-spliced α_{1C} with caveolin-3 in cardiac myocytes. (*A*, *Upper*) Confocal images of cardiac myocytes depicting colocalization of endogenous α_{1C} (anti-α_{1C}, green) and endogenous caveolin-3 (anti–caveolin-3, red). (*A*, *Lower*) Significant α_{1C} /caveolin-3 colocalization is also found in myocytes expressing intein-spliced α_{1C} (anti-GFP, green). (Scale bar, 20 μm.) (*B*) Quantitation of colocalization shown in *A*. Colocalization coefficient of pixels in the green (α_{1C}) and red (caveolin-3) channels was calculated using the JaCoP plugin in ImageJ from images acquired from 20 individual cells. Pearson's coefficient data depict robust α_{1C}/caveolin-3 colocalization between control (uninfected) and recombinant (expressing intein-spliced α_{1C}) myocytes. *P6E-11 through unpaired *t* test. (*C*) Quantitation of α_{1C}/ryanodine receptor (RyR) (shown in Fig. 4*D*) and α_{1C}/caveolin (shown here in *A* and *B*) as measured through Li's intensity correlation coefficient using the JaCoP plugin on the same images analyzed in Fig.4 *D* and *E* and Fig. S3 *A* and *B*). Similar results to that obtained through Pearson's correlation corroborate strong colocalization between α_{1C}/RyR and α_{1C}/caveolin-3 in both uninfected (control) and adenovirally infected (expressing intein-spliced α_{1C}) myocytes. *P1.2E-10 through unpaired *t* test.

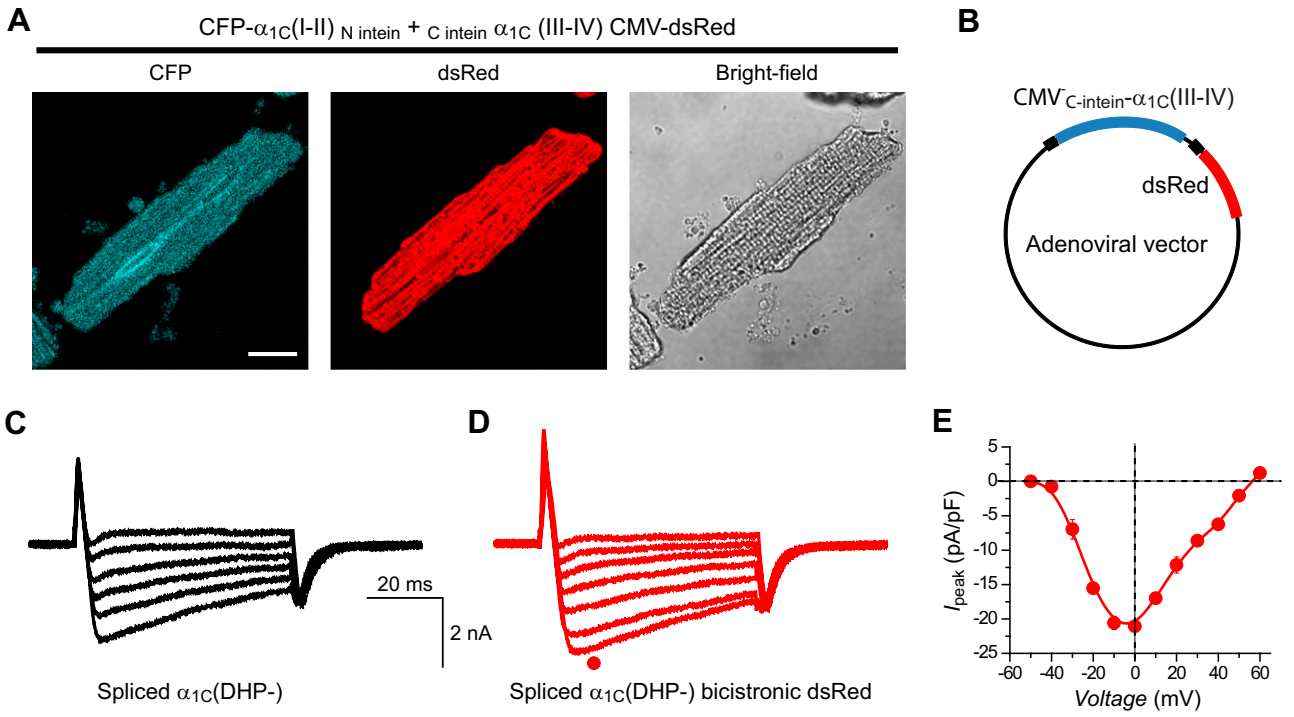

Fig. S5. Characterization of intein-spliced dihydropyridine (DHP)-insensitive α_{1C} expressed in bicistronic vectors in cardiac myocytes. (*A*) Confocal images of myocytes expressing intein-spliced CFP-tagged intein-spliced α_{1C} and dsRed from a bicistronic vector. (Scale bar, 20 μm.) (*B*) Construction of the $_{C\text{-intein}}\alpha_{1C}$III–IV_dsRed biscistronic vector. dsRed expression is under the control of a separate CMV promoter. (*C*) Exemplar current traces from cells expressing intein-spliced CFP/YFP-tagged DHP-insensitive α_{1C} $n = 8$. (*D*) Exemplar current traces and (*E*) population current-voltage (*J–V*) relationships from myocytes expressing intein-spliced DHP-insensitive α_{1C} channels ($n = 7$) with bicistronic dsRed. Intein-spliced DHP– α_{1C} derived from bicistronic dsRed constructs exhibit large whole-cell Ba^{2+} current in presence of Nifedipine. Similar current traces, *C* and *D* indicate that YFP fusion on C terminus of the channels does not affect function.

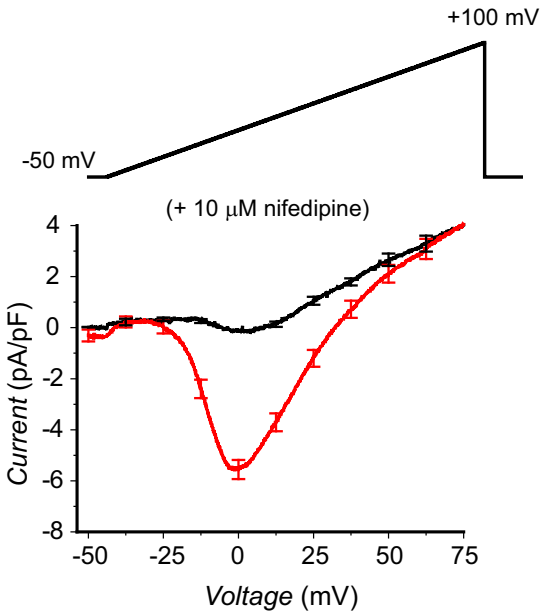

Fig. S6. Nifedipine-based separation of WT and DHP-resistant α_{1C} in cardiac myocytes expressing intein-spliced α_{1C} by using a –50 mV holding potential and 2 mM Ca^{2+} as charge carrier. Under these conditions, WT $Ca_V1.2$ whole-cell currents elicited by a ramp protocol were deeply inhibited by 10 μM nifedipine (black trace, $n = 4$), whereas myocytes expressing intein-spliced DHP-resistant α_{1C} (red trace, $n = 3$) displayed a sevenfold larger remnant current.

Table S1. Gating parameters for WT and intein-spliced $Ca_V1.2$ channels

Channel type	G pApF^{-1}·mV^{-1}	$V_{0.5}$ mV	k mV	n
$\alpha_{1C} + \beta_{2a}$	0.58 ± 0.21	−11.20 ± 1.06	5.67 ± 0.3	7
Spliced WT $\alpha_{1C} + \beta_{2a}$	0.48 ± 0.15	−11.99 ± 1.10	6.99 ± 1.00	7
Spliced α_{1C}[TQ/YM] + β_{2a}	0.52 ± 0.11	−9.66 ± 0.82	5.5 ± 0.16	11

I–V relations were fit to the following equation:

$$I = G(V - V_{rev})\frac{1}{1 + exp(\frac{V_{0.5} - V}{k})},$$

where I is the whole-cell current density (pA/pF), G is the specific conductance (pA pF-1 mV-1), V_{rev} is the reversal potential (mV), $V_{0.5}$ is the voltage of half-maximal activation (mV), and k is a slope factor (mV).

Table S2. Accession numbers of cDNAs

GenBank ID	Gene name	Accession no.
α_{1C}($Ca_V1.2$) rabbit cardiac	CACNA1C/CACH2C	X15539.1
β2a rat cardiac/brain	Cacnb2	M80545.1
N. punctiforme PCC73102 DnaE-n intein	Npun_F4872	ZP_00111398.2
N. punctiforme PCC73102 DnaE-c intein	Npun_F5684	ZP_00108882.1

Table S3. List and sequences of cloning primers

Primer no.	Sequence 5′–3′	Included restriction or in-fusion site
1	ACCCGGAGGAGCACGTTCGAC	
2	TTCATAGCTTAAACAGGGCTGGAGGTCATCCATGTTGATCTTGGTG	
3	TGGATGACCTCCAGCCCTGTTTAAGCTATGAAACGGAAATATTG	
4	AAACGGGCCCTCTAGATTAATTCGGCAAATTATC	XbaI
5	ATATAAGCTTGCCACCATGGTGAGCAAGGGCGAGGAGCTGTTCACCGGGGTG	HindIII
6	TCGAAGCATTGTCAGCTTGTACAGCTCGTCCATGCCGAGAGTGATC	
7	GACGAGCTGTACAAGCTGACAATGCTTCGAGCCCTTGTTCAGCCAG	
8	ATGGGGTTCTTCAGGGTGAGG	
9	ATATGGTACCATGGGAATCAAAATAGCCACACG	KpnI
10	CTTATCCTCACTCTCATTGAAACAATTAGAAGCTATGAAGCCATT	
11	TCTAATTGTTTCAATGAGAGTGAGGATAAGAGTCCCTACCCCAAC	
12	ACTCGGTAGTTGTAGATAGGG	
13	ATATGGTACCATGGGAATCAAAATAG	KpnI
14	CATCAGCAGCGTGTAGACAATCACGATGTTCCCAATGGTCCGGATG	
15	TACACGCTGCTGATGTTCATGTTCGCCTGCATCGGAGTCCAGCTC	
16	AGCAGGATGAGGACGAACATCAGG	
17	ATATGGTACCGCCACCATGGTGAGCAAGGG	KpnI
18	ATATCTCGAGTTAATTCGGCAAATTATCAACCCG	XhoI
19	ATATGGTACCGCCACCATGGGAATCAAAATAGCCAC	KpnI
20	ATATCTCGAGTTACTTGTACAGCTCGTCCATG	XhoI
21	GTAACTATAACGGTCGCCACCATGGGAATCAAAATAGCCACACG	In-fusion, GTAACTATAACGGTC
22	ATTACCTCTTTCTCCTTAAGACAGGCTGCTGACGCCGGCCCTGCGGTCC	In-fusion, ATTACCTCTTTCTCC

Sleep Drives Metabolite Clearance from the Adult Brain

Lulu Xie *et al.*

Science **342**, 373 (2013);
DOI: 10.1126/science.1241224

Science (print ISSN 0036-8075; online ISSN 1095-9203) is published weekly, except the last week in December, by the American Association for the Advancement of Science, 1200 New York Avenue NW, Washington, DC 20005.

Sleep Drives Metabolite Clearance from the Adult Brain

Lulu Xie,[1]* Hongyi Kang,[1]* Qiwu Xu,[1] Michael J. Chen,[1] Yonghong Liao,[1] Meenakshisundaram Thiyagarajan,[1] John O'Donnell,[1] Daniel J. Christensen,[1] Charles Nicholson,[2] Jeffrey J. Iliff,[1] Takahiro Takano,[1] Rashid Deane,[1] Maiken Nedergaard[1]†

The conservation of sleep across all animal species suggests that sleep serves a vital function. We here report that sleep has a critical function in ensuring metabolic homeostasis. Using real-time assessments of tetramethylammonium diffusion and two-photon imaging in live mice, we show that natural sleep or anesthesia are associated with a 60% increase in the interstitial space, resulting in a striking increase in convective exchange of cerebrospinal fluid with interstitial fluid. In turn, convective fluxes of interstitial fluid increased the rate of β-amyloid clearance during sleep. Thus, the restorative function of sleep may be a consequence of the enhanced removal of potentially neurotoxic waste products that accumulate in the awake central nervous system.

Despite decades of effort, one of the greatest mysteries in biology is why sleep is restorative and, conversely, why lack of sleep impairs brain function (*1*, *2*). Sleep deprivation reduces learning, impairs performance in cognitive tests, prolongs reaction time, and is a common cause of seizures (*3*, *4*). In the most extreme case, continuous sleep deprivation kills rodents and flies within a period of days to weeks (*5*, *6*). In humans, fatal familial or sporadic insomnia is a progressively worsening state of sleeplessness that leads to dementia and death within months or years (*7*).

Proteins linked to neurodegenerative diseases, including β-amyloid (Aβ) (*8*), α-synuclein (*9*), and tau (*10*), are present in the interstitial space surrounding cells of the brain. In peripheral tissue, lymph vessels return excess interstitial proteins to the general circulation for degradation in the liver (*11*). Yet despite its high metabolic rate and the fragility of neurons to toxic waste products, the brain lacks a conventional lymphatic system. Instead, cerebrospinal fluid (CSF) recirculates through the brain, interchanging with interstitial fluid (ISF) and removing interstitial proteins, including Aβ (*12*, *13*). The convective exchange of CSF and ISF is organized around the cerebral vasculature, with CSF influx around arteries, whereas ISF exits along veins. These pathways were named the glymphatic system on the basis of their dependence on astrocytic aquaporin-4 (AQP4) water channels and the adoption of functions homologous to peripheral lymphatic removal of interstitial metabolic byproducts (*14*). Deletion of AQP4 channels reduces clearance of exogenous Aβ by 65%, suggesting that convective movement of ISF is a substantial contributor to the removal of interstitial waste products and other products of cellular activity (*12*). The interstitial concentration of Aβ is higher in awake than in sleeping rodents and humans, possibly indicating that wakefulness is associated with increased Aβ production (*15*, *16*). We tested the alternative hypothesis that Aβ clearance is increased during sleep and that the sleep-wake cycle regulates glymphatic clearance.

We used in vivo two-photon imaging to compare CSF influx into the cortex of awake, anesthetized, and sleeping mice. The fluorescent tracers were infused into the subarachnoid CSF via a cannula implanted in the cisterna magna for real-time assessment of CSF tracer movement. Electrocorticography (ECoG) and electromyography (EMG) were recorded in order to continuously monitor the state of brain activity (Fig. 1A and fig. S1). In initial experiments, the volume and rate of tracer infusion were adjusted so as to avoid changes in behavior state or ECoG (fig. S1). Because mice sleep much of the day, a small molecular weight tracer, fluorescein isothiocyanate (FITC)–dextran (3 kD) in aCSF, was infused at midday (12 to 2 p.m.) via the cannula implanted in the cisterna magna. In sleeping mice, a robust influx of the fluorescent CSF tracer was noted along periarterial spaces, in the subpial regions, and in the brain parenchyma similar to previous findings in anesthetized mice (Fig. 1, B and C, and fig. S2) (*12*). ECoG power spectrum analysis depicted a relatively high power of slow waves that is consistent with sleep (Fig. 1D). CSF tracer infusion (Texas red-dextran, 3 kD) was repeated in the same mouse after it was awakened through gentle handling of its tail. Unexpectedly, arousal sharply reduced tracer influx compared with that of the sleeping state. Periarterial and parenchymal tracer influx was reduced by ~95% in awake as compared with sleeping mice during the 30-min imaging session (Fig. 1, B and C, and fig. S2). ECoG showed a reduction in the relative prevalence of slow (delta) waves concomitant with a significant increase in the power of fast activity, confirming that the animals were awake ($n = 6$ mice, $P < 0.05$, paired t test) (Fig. 1D). To investigate whether the state of brain activity indeed controlled CSF influx, we repeated the experiments in a new cohort of mice in which all experiments were performed when the animals were awake (8 to 10 p.m.). Because mice normally do not sleep at this time of day, we first evaluated CSF tracer influx in the awake state by means of intracisternal infusion of FITC-dextran. CSF tracer influx into the brain was largely absent and only slowly gained access to the superficial cortical layers (Fig. 1, E and F, and fig. S2). After 30 min imaging of CSF tracer in the awake state, the animals were anesthetized with intraperitoneal administration of ketamine/xylazine (KX). Texas red-dextran was administered 15 min later, when a stable increase in slow wave activity was noted (Fig. 1, E and F). Texas red-dextran rapidly flushed in along periarterial spaces and entered the brain parenchyma at a rate comparable with that of naturally sleeping mice (Fig. 1, B and E). Ketamine/xylazine anesthesia significantly increased influx of CSF tracer in all mice analyzed [$n = 6$ mice, $P < 0.05$, two-way analysis of variance (ANOVA) with Bonferroni test], which was concomitant with a significant increase in the power of slow wave activity ($n = 6$ mice, $P < 0.05$, paired t test) (Fig. 1, G and F). Thus, glymphatic CSF influx is sharply suppressed in conscious alert mice as compared with naturally sleeping or anesthetized littermates.

Influx of CSF is in part driven by arterial pulse waves that propel the movement of CSF inward along periarterial spaces (*12*). It is unlikely that diurnal fluctuations in arterial pulsation are responsible for the marked suppression of convective CSF fluxes during wakefulness because arterial blood pressure is higher during physical activity. An alternative possibility is that the awake brain state is linked to a reduction in the volume of the interstitial space because a constricted interstitial space would increase resistance to convective fluid movement and suppress CSF influx. To assess the volume and tortuosity of the interstitial space in awake versus sleeping mice, we used the real-time iontophoretic tetramethylammonium (TMA) method in head-fixed mice (Fig. 2A and fig. S3) (*17*, *18*). TMA recordings in cortex of sleeping mice collected at midday (12 to 2 p.m.) confirmed that the interstitial space volume fraction (α) averaged 23.4 ± 1.9% ($n = 6$ mice) (*19*). However, the interstitial volume fraction was only 14.1 ± 1.8% in awake mice recorded at 8 to 10 p.m. ($n = 4$ mice, $P < 0.01$, t test) (Fig. 2B). Analysis of cortical ECoG recorded by the TMA reference electrode confirmed that the power of slow wave activity was higher in sleeping than in awake mice, which is concurrent with a lower power of high-frequency activity (Fig. 2C).

To further validate that the volume of the interstitial space differed in awake versus sleeping mice, we also obtained TMA recordings in awake mice in the late evening (8 to 10 p.m.) and repeated the recordings in the same mice after administration of ketamine/xylazine. This approach,

[1]Division of Glial Disease and Therapeutics, Center for Translational Neuromedicine, Department of Neurosurgery, University of Rochester Medical Center, Rochester, NY 14642, USA. [2]Department of Neuroscience and Physiology, Langone Medical Center, New York University, New York, NY 10016, USA.

*These authors contributed equally to this work.

†Corresponding author. E-mail: nedergaard@urmc.rochester.edu

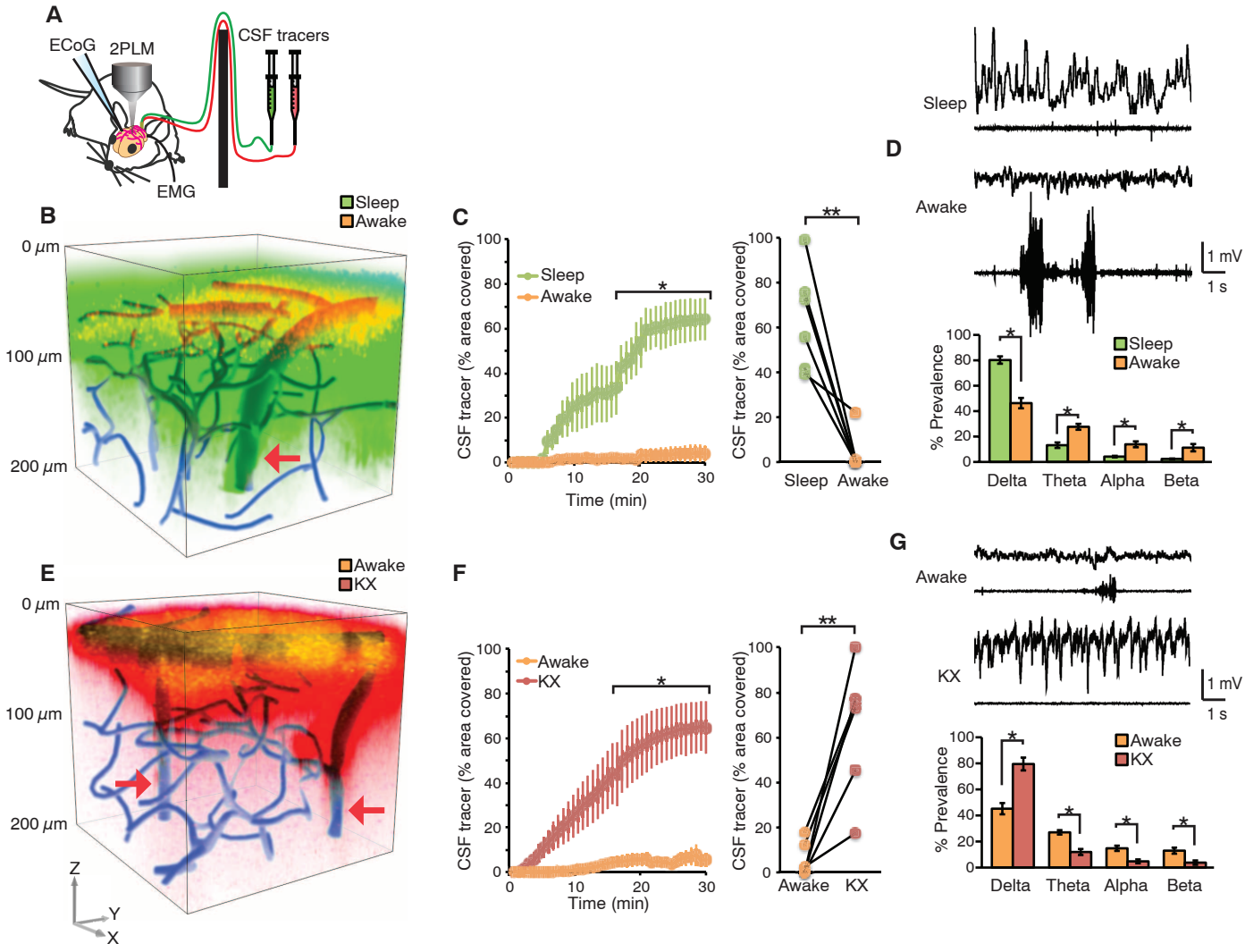

Fig. 1. Wakefulness suppresses influx of CSF tracers. (**A**) Diagram of experimental setup used for two-photon imaging of CSF tracer movement in real time. To avoid disturbing the state of brain activity, a cannula with dual ports was implanted in the cisterna magna for injection of CSF tracers. ECoG and EMG were recorded to monitor the state of brain activity. (**B**) Three-dimensional (3D) vectorized reconstruction of the distribution of CSF tracers injected in a sleeping mouse and then again after the mouse was awakened. The vasculature was visualized by means of cascade blue-dextran administered via the femoral vein. FITC-dextran (green) was first injected in the cisterna magna in a sleeping mouse and visualized by collecting repeated stacks of z-steps. Thirty min later, the mouse was awakened by gently moving its tail, and Texas red-dextran (red) was administered 15 min later. The experiments were performed mostly asleep (12 to 2 p.m.). The arrow points to penetrating arteries. (**C**) Comparison of time-dependent CSF influx in sleep versus awake. Tracer influx was quantified 100 μm below the cortical surface; $n = 6$ mice; $^{*}P < 0.05$, two-way ANOVA with Bonferroni test. (Right) The tracer intensity within the two arousal states at the 30-min time point was compared. $^{**}P < 0.01$, t test. (**D**) ECoG and EMG recordings acquired during sleep and after the mouse was awakened. Power spectrum analysis of all the animals analyzed in the two arousal states ($n = 6$ mice; $^{*}P < 0.05$, t test). (**E**) 3D reconstruction of CSF tracer influx into the mouse cortex. FITC-dextran was first injected in the awake stage, and cortical influx was visualized by means of two-photon excitation for 30 min. The mouse was then anesthetized with ketamine/xylazine (intraperitoneally), and Texas red-dextran was injected intracisternally 15 min later. The vasculature was visualized by means of cascade blue-dextran. Arrows point to penetrating arteries. (**F**) Comparison of time-dependent CSF influx in awake versus ketamine/xylazine anesthesia; $n = 6$ mice; $^{*}P < 0.05$, two-way ANOVA with Bonferroni test. (Right) The tracer intensity during the two arousal states at the 30-min time point was compared. $^{**}P < 0.01$, t test. (**G**) ECoG and EMG recordings in the awake mouse and after administration of ketamine/xylazine. Power spectrum analysis of all the animals analyzed in the two arousal states; $n = 6$ mice; $^{*}P < 0.05$, t test.

which eliminated interanimal variability in electrode placement and TMA calibration, showed that anesthesia consistently increased the interstitial space volume fraction by >60%, from 13.6 ± 1.6% for awake mice to 22.7 ± 1.3% in the same mice after they received ketamine/xylazine ($n = 10$ mice, $P < 0.01$, paired t test) (Fig. 2D). Analysis of ECoG activity extracted from the TMA reference electrode showed that ketamine/xylazine increased the power of slow wave activity in all animals analyzed (Fig. 2E). Thus, the cortical interstitial volume fraction is 13 to 15% in the awake state as compared to 22 to 24% in sleeping or anesthetized mice. Tortuosity of the interstitial space did not differ significantly according to changes in the state of brain activity; awake, sleeping, and anesthetized mice all exhibited a λ value in the range of 1.3 to 1.8, which is consistent with earlier reports ($n = 4$ to 10 mice, $P > 0.1$, t test) (Fig. 2, B and D) (*19*–*21*). Recordings obtained 300 μm below the cortical surface did not differ significantly from those obtained at 150 μm, suggesting that preparation of the cranial window was not associated with tissue injury ($n = 6$ mice, $P > 0.4$, t test) (Fig. 2D and fig. S3D). Other reports have shown that the interstitial volume is ~19% in anesthetized young mice but declines to ~13% in

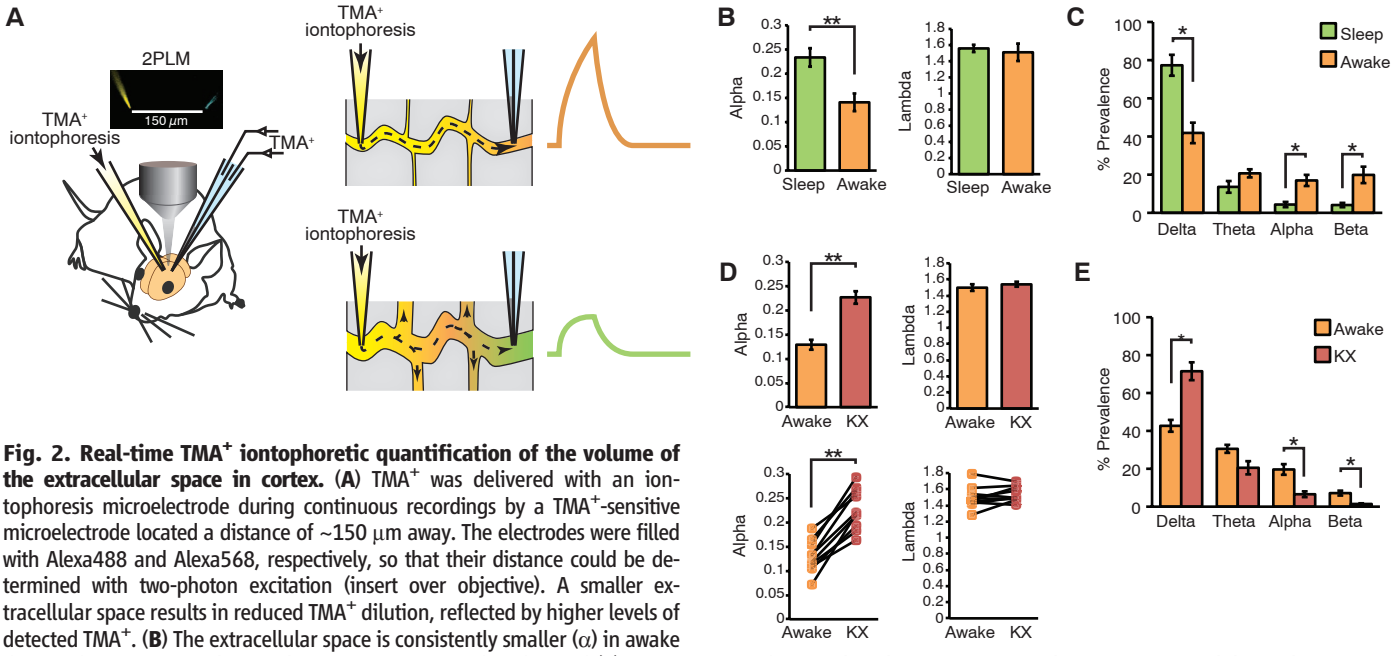

Fig. 2. Real-time TMA$^+$ iontophoretic quantification of the volume of the extracellular space in cortex. (**A**) TMA$^+$ was delivered with an iontophoresis microelectrode during continuous recordings by a TMA$^+$-sensitive microelectrode located a distance of ~150 μm away. The electrodes were filled with Alexa488 and Alexa568, respectively, so that their distance could be determined with two-photon excitation (insert over objective). A smaller extracellular space results in reduced TMA$^+$ dilution, reflected by higher levels of detected TMA$^+$. (**B**) The extracellular space is consistently smaller (α) in awake than in sleeping mice, whereas the tortuosity remained unchanged (λ); $n = 4$ to 6 mice; $^{**}P < 0.01$, t test. (**C**) Power spectrum analysis of ECoG recordings; $n = 6$ mice; $^{*}P < 0.05$, t test. (**D**) The extracellular space was consistently smaller in the awake state than after administration of ketamine/xylazine in paired recordings within the same mouse, whereas tortuosity did not change after anesthesia; $n = 10$ mice; $^{**}P < 0.01$, t test. (Bottom) TMA measurements obtained during the two arousal states compared for each animal. (**E**) Power spectrum analysis of ECoG; $n = 6$ mice; *P < 0.05, t test.

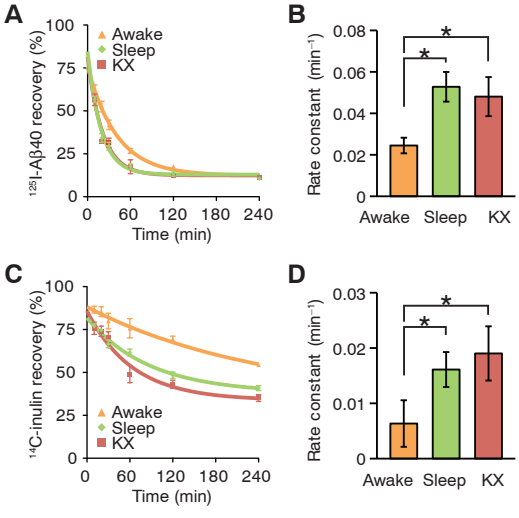

Fig. 3. Sleep improves clearance of Aβ. (**A**). Time-disappearance curves of ^{125}I-Aβ$_{1\text{-}40}$ after its injection into the frontal cortex in awake (orange triangles), sleeping (green diamonds), and anesthetized (red squares, ketamine/xylazine) mice. (**B**) Rate constants derived from the clearance curves. (**C**) Time-disappearance curves of ^{14}C-inulin after its injection into the frontal cortex of awake (orange triangles), sleeping (green diamonds), and anesthetized (red squares, ketamine/xylazine) mice. (**D**) Rate constants derived from the clearance curves. A total of 77 mice were included in the analysis: 25 awake, 29 asleep, and 23 anesthetized, with 3 to 6 mice per time point. $^{*}P < 0.05$ compared with awake, ANOVA with Bonferroni test.

aged mice (*22*). Collectively, these observations support the notion that influx of CSF tracers is suppressed in awake mice as a result of contraction of the interstitial space: The smaller space during wakefulness increases tissue resistance to interstitial fluid flux and inward movement of CSF. This effect of arousal state on interstitial volume likely holds major implications for diffusion of neurotransmitters, such as glutamate (*23*).

Because previous analysis indicates that as much as 65% of exogenously delivered Aβ is cleared by the glymphatic system (*12*), we tested whether interstitial Aβ is cleared most efficiently during sleep. Radiolabeled ^{125}I-Aβ$_{1\text{-}40}$ was injected intracortically in three groups of animals: freely behaving awake mice, naturally sleeping mice, and animals anesthetized with ketamine/xylazine (fig. S4). Brains were harvested 10 to 240 min later for analysis of ^{125}I-Aβ retention. Aβ was cleared twofold faster in the sleeping mice as compared with the awake mice ($n = 23$ to 29 mice, $P < 0.05$, ANOVA with Bonferroni test) (Fig. 3, A and B, $P < 0.05$). Aβ clearance did not differ between sleeping and anesthetized mice. Because Aβ is also removed from CNS via receptor-mediated transport across the blood-brain barrier (*24*), we also analyzed the clearance of an inert tracer, ^{14}C-inulin. ^{14}C-inulin was cleared more efficiently (greater than twofold) in sleeping and anesthetized mice as compared with awake mice (Fig. 3, C and D).

What drives the brain state–dependent changes of the interstitial space volume? The observation that anesthesia increases glymphatic influx and efflux (Figs. 1 and 3), suggests that it is not circadian rhythm but rather the sleep-wake state itself that determines the volume of the interstitial space and therefore the efficiency of glymphatic solute clearance. Arousal is driven by the concerted release of neuromodulators (*25*). In particular, locus coeruleus–derived noradrenergic signaling appears critical for driving cortical networks into the awake state of processing (*26*, *27*). In peripheral tissues, such as kidney and heart, noradrenaline regulates the activity of membrane transporters and channels that control cell volume (*28*). We hypothesized that adrenergic signaling in the awake state modifies cell volume and thus the size of the interstitial space. We first assessed whether suppression of adrenergic signaling in the awake conscious brain can enhance glymphatic tracer influx by pretreating awake mice with a cocktail of adrenergic receptor antagonists or vehicle (aCSF) 15 min before infusion of fluorescent CSF tracers (*27*). The adrenergic receptor antagonists were administered through a cannula inserted into the cisterna magna, with an initial bolus followed by slow continuous drug infusion. Administration of adrenergic antagonists induced an increase in CSF tracer influx, resulting in rates of CSF tracer influx that were more comparable with influx observed during sleep or anesthesia than in the awake state (Fig. 4, A and B, and fig. S5). We asked whether increases in the level of norepinephrine (NE) resulting from stress during restraining at the microscope stage affected the observations. Microdialysis samples

of the interstitial fluid showed that the NE concentration did not increase in trained mice during restraining but that NE, as expected, fell after administration of ketamine/xylazine (Fig. 4C).

We next evaluated whether adrenergic receptor inhibition increased interstitial volume in the same manner as sleep and anesthesia. We used the TMA method to quantify the effect of local adrenergic inhibition on the volume of the interstitial space. To restrict adrenergic inhibition to the cortex, receptor antagonists were applied directly to the exposed cortical surface rather than intracisternal delivery. TMA recordings showed that inhibition of adrenergic signaling in cortex increased the interstitial volume fraction from 14.3 ± 5.2% to 22.6 ± 1.2% (n = 4 to 8 mice, P < 0.01, t test). Interstitial volume was significantly greater than in awake littermates exposed to vehicle (aCSF) (P < 0.01) but comparable with the interstitial volume in sleeping or anesthetized mice (P = 0.77 and P = 0.95, respectively, t test) (Fig. 4D). Cortical ECoG displayed an increase in the power of slow waves when exposed to adrenergic receptor antagonists (n = 7 mice, P < 0.01, one-way ANOVA with Bonferroni test). In accordance with earlier findings (*27*), analysis of the power spectrum showed that inhibition of adrenergic signaling transformed the cortical ECoG of awake mice into a more sleep-like, albeit less regular, profile (Fig. 4E). These analyses suggest that adrenergic signaling plays an important role in modulating not only cortical neuronal activity but also the volume of the interstitial space. NE triggers rapid changes in neural activity (*27*, *28*), which in turn can modulate the volume of the interstitial space volume (*29*). Nevertheless, additional analysis is clearly required to determine which cell types contribute to expansion of the interstitial space volume during sleep, anesthesia, or blockade of NE receptors (Figs. 2, B to D, and 4D).

Because of the high sensitivity of neural cells to their environment, it is essential that waste products of neural metabolism are quickly and efficiently removed from the brain interstitial space. Several degradation products of cellular activity, such as Aβ oligomers and amyloid depositions, have adverse effects on synaptic transmission (*30*) and cytosolic Ca^{2+} concentrations (*31*) and can trigger irreversible neuronal injury (*32*). The existence of a homeostatic drive for sleep—including accumulation of a "need to sleep" substance during wakefulness that dissipates during sleep—has been proposed (*33*). Because biological activity is inevitably linked to the production of metabolic degradation products, it is possible that sleep subserves the important function of clearing multiple poten-

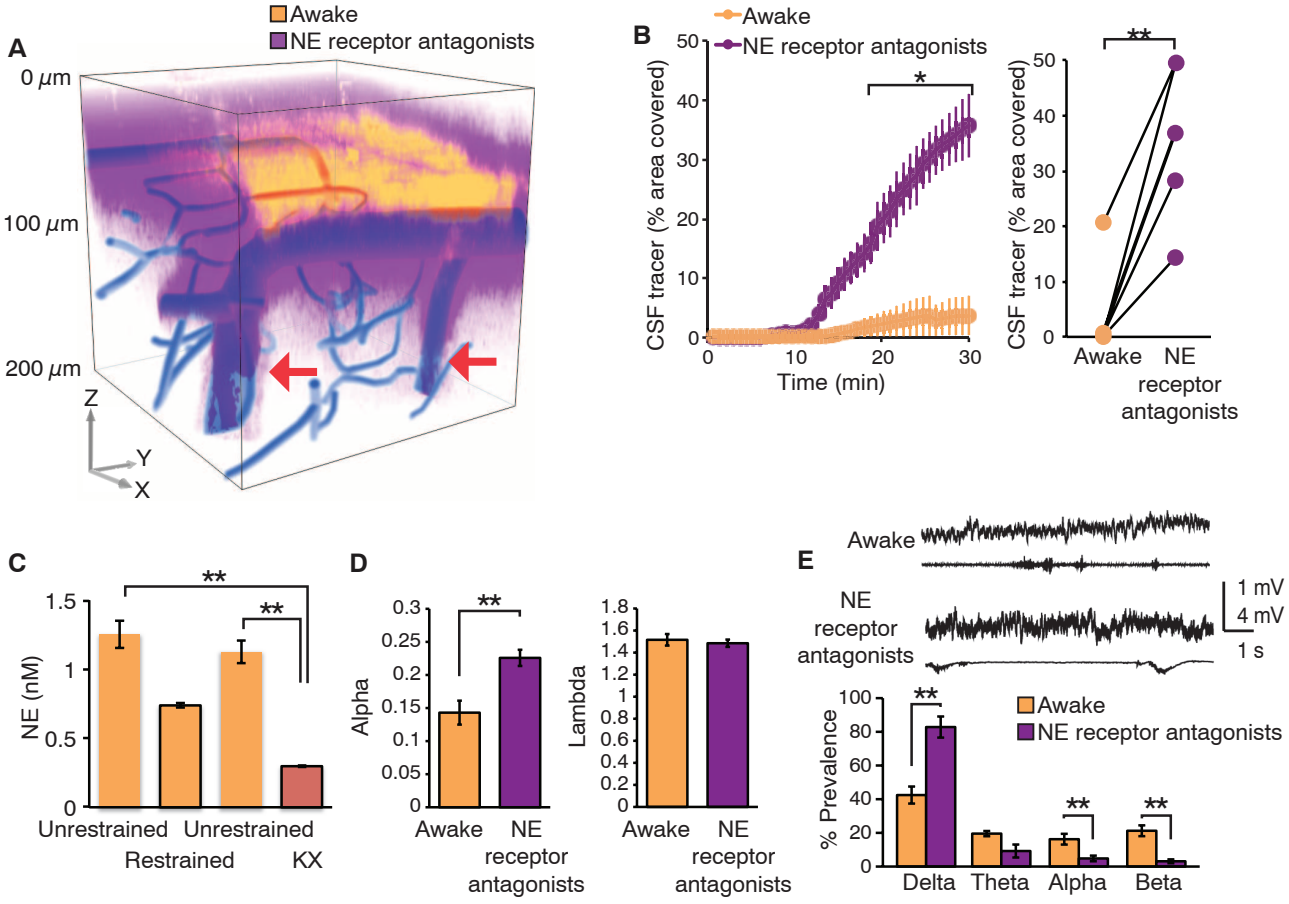

Fig. 4. Adrenergic inhibition increases CSF influx in awake mice. (**A**) CSF tracer influx before and after intracisternal administration of a cocktail of adrenergic receptor antagonists. FITC-dextran (yellow, 3 kD) was first injected in the cisterna magna in the awake mouse, and cortical tracer influx was visualized by means of two-photon excitation for 30 min. The adrenergic receptor antagonists (prazosin, atipamezole, and propranolol, each 2 mM) were then slowly infused via the cisterna magna cannula for 15 min followed by injection of Texas red-dextran (purple, 3 kD). The 3D reconstruction depicts CSF influx 15 min after the tracers were injected in cisterna magna. The vasculature was visualized by means of cascade blue-dextran. Arrows point to penetrating arteries. (**B**) Comparison of tracer influx as a function of time before and after administration of adrenergic receptor antagonists. Tracer influx was quantified in the optical section located 100 μm below the cortical surface; n = 6 mice; *P < 0.05, two-way ANOVA with Bonferroni test. (Right) The tracer intensity during the two arousal states at the 30-min time point was compared. **P < 0.01, t test. (**C**) Comparison of the interstitial concentration of NE in cortex during head-restraining versus unrestrained (before and after), as well as after ketamine/xylazine anesthesia. Microdialysis samples were collected for 1 hour each and analyzed by using high-performance liquid chromatography. **P < 0.01, one-way ANOVA with Bonferroni test. (**D**) TMA^+ iontophoretic quantification of the volume of the extracellular space before and after adrenergic inhibition; n = 4 to 8 mice; **P < 0.01, t test. (**E**) Power spectrum analysis, n = 7 mice; **P < 0.01, one-way ANOVA with Bonferroni test.

tially toxic CNS waste products. Our analysis indicates that the cortical interstitial space increases by more than 60% during sleep, resulting in efficient convective clearance of Aβ and other compounds (Figs. 2 and 3). The purpose of sleep has been the subject of numerous theories since the time of the ancient Greek philosophers (*34*). An extension of the findings reported here is that the restorative function of sleep may be due to the switching of the brain into a functional state that facilitates the clearance of degradation products of neural activity that accumulate during wakefulness.

References and Notes

1. C. B. Saper, P. M. Fuller, N. P. Pedersen, J. Lu, T. E. Scammell, *Neuron* **68**, 1023–1042 (2010).
2. J. A. Hobson, *Nature* **437**, 1254–1256 (2005).
3. B. A. Malow, *Epilepsy Curr.* **4**, 193–195 (2004).
4. R. Stickgold, *Nature* **444**, 559–560 (2006).
5. A. Rechtschaffen, M. A. Gilliland, B. M. Bergmann, J. B. Winter, *Science* **221**, 182–184 (1983).
6. P. J. Shaw, G. Tononi, R. J. Greenspan, D. F. Robinson, *Nature* **417**, 287–291 (2002).
7. P. Montagna, P. Gambetti, P. Cortelli, E. Lugaresi, *Lancet Neurol.* **2**, 167–176 (2003).
8. J. R. Cirrito *et al.*, *Neuron* **48**, 913–922 (2005).
9. M. E. Larson *et al.*, *J. Neurosci.* **32**, 10253–10266 (2012).
10. K. Yamada *et al.*, *J. Neurosci.* **31**, 13110–13117 (2011).
11. K. Aukland, R. K. Reed, *Physiol. Rev.* **73**, 1–78 (1993).
12. J. J. Iliff *et al.*, *Sci. Transl. Med.* **4**, 147ra111 (2012).
13. J. J. Iliff *et al.*, *J. Clin. Invest.* **123**, 1299–1309 (2013).
14. M. Nedergaard, *Science* **340**, 1529–1530 (2013).
15. R. J. Bateman *et al.*, *Nat. Med.* **12**, 856–861 (2006).
16. J. E. Kang *et al.*, *Science* **326**, 1005–1007 (2009).
17. C. Nicholson, J. M. Phillips, *J. Physiol.* **321**, 225–257 (1981).
18. C. Nicholson, *J. Neurosci. Methods* **48**, 199–213 (1993).
19. X. Yao, S. Hrabetová, C. Nicholson, G. T. Manley, *J. Neurosci.* **28**, 5460–5464 (2008).
20. C. Nicholson, E. Syková, *Trends Neurosci.* **21**, 207–215 (1998).
21. E. Syková, C. Nicholson, *Physiol. Rev.* **88**, 1277–1340 (2008).
22. E. Syková *et al.*, *Proc. Natl. Acad. Sci. U.S.A.* **102**, 479–484 (2005).
23. J. P. Kinney *et al.*, *J. Comp. Neurol.* **521**, 448–464 (2013).
24. R. Deane *et al.*, *J. Clin. Invest.* **118**, 4002–4013 (2008).
25. M. Steriade, D. A. McCormick, T. J. Sejnowski, *Science* **262**, 679–685 (1993).
26. M. E. Carter *et al.*, *Nat. Neurosci.* **13**, 1526–1533 (2010).
27. C. M. Constantinople, R. M. Bruno, *Neuron* **69**, 1061–1068 (2011).
28. J. O'Donnell, D. Zeppenfeld, E. McConnell, S. Pena, M. Nedergaard, *Neurochem. Res.* **37**, 2496–2512 (2012).
29. C. J. McBain, S. F. Traynelis, R. Dingledine, *Science* **249**, 674–677 (1990).
30. K. Parameshwaran, M. Dhanasekaran, V. Suppiramaniam, *Exp. Neurol.* **210**, 7–13 (2008).
31. K. V. Kuchibhotla *et al.*, *Neuron* **59**, 214–225 (2008).
32. M. P. Mattson, *Ann. N. Y. Acad. Sci.* **747**, 50–76 (1994).
33. A. Borbely, I. Tobler, in *Brain Mechanisms of Sleep*, D. J. McGinty, Ed. (Raven, New York, 1985), pp. 35–44.
34. J. Barbera, *Sleep Med.* **9**, 906–910 (2008).

Acknowledgments: This study was supported by NIH/National Institute of Neurological Disorders and Stroke (NS078167 and NS078304 to M.N. and NS028642 to C.N.). We thank S. Veasey for comments on the manuscript.

Supplementary Materials

www.sciencemag.org/content/342/6156/373/suppl/DC1
Materials and Methods
Figs. S1 to S5
References

30 May 2013; accepted 28 August 2013
10.1126/science.1241224

Reading Literary Fiction Improves Theory of Mind

David Comer Kidd* and Emanuele Castano*

Understanding others' mental states is a crucial skill that enables the complex social relationships that characterize human societies. Yet little research has investigated what fosters this skill, which is known as Theory of Mind (ToM), in adults. We present five experiments showing that reading literary fiction led to better performance on tests of affective ToM (experiments 1 to 5) and cognitive ToM (experiments 4 and 5) compared with reading nonfiction (experiments 1), popular fiction (experiments 2 to 5), or nothing at all (experiments 2 and 5). Specifically, these results show that reading literary fiction temporarily enhances ToM. More broadly, they suggest that ToM may be influenced by engagement with works of art.

The capacity to identify and understand others' subjective states is one of the most stunning products of human evolution. It allows successful navigation of complex social relationships and helps to support the empathic responses that maintain them (*1*–*5*). Deficits in this set of abilities, commonly referred to as Theory of Mind (ToM), are associated with psychopathologies marked by interpersonal difficulties (*6*–*8*). Even when the ability is intact, disengagement of ToM has been linked to the breakdown of positive interpersonal and intergroup relationships (*9*).

Researchers have distinguished between affective ToM (the ability to detect and understand others' emotions) and cognitive ToM (the inference and representation of others' beliefs and intentions) (*7*, *8*). The affective component of ToM, in particular, is linked to empathy (positively) and antisocial behavior (negatively) (*7*, *8*). It is thus not surprising that we foster ToM in our children by having them attend to the emotional states of others: "Do you think he is happy or sad as a consequence of your action?" Such explicit encouragements to understand others usually diminish when children appear to skillfully and empathically engage in interpersonal relationships. Cultural practices, though, may function to promote and refine interpersonal sensitivity throughout our lives. One such practice is reading fiction.

Familiarity with fiction, self-reported empathy, and performance on an advanced affective ToM test have been correlated (*10*, *11*), and limited experimental evidence suggests that reading fiction increases self-reported empathy (*12*, *13*). Fiction seems also to expand our knowledge of others' lives, helping us recognize our similarity to them (*10*, *11*, *14*). Although fiction may explicitly convey social values and reduce the strangeness of others, the observed relation between familiarity with fiction and ToM may be due to more subtle characteristics of the text. That is, fiction may change how, not just what, people think about others (*10*, *11*, *14*). We submit that fiction affects ToM processes because it forces us to engage in mind-reading and character construction. Not any kind of fiction achieves that, though. Our proposal is that it is literary fiction that forces the reader to engage in ToM processes.

The category of literary fiction has been contested on the grounds that it is merely a marker of social class, but features of the modern literary novel set it apart from most best-selling thrillers or romances. Miall and Kuiken (*15*–*17*) emphasize that through the systematic use of phonological, grammatical, and semantic stylistic devices, literary fiction defamiliarizes its readers. The capacity of literary fiction to unsettle readers' expectations and challenge their thinking is also reflected in Roland Barthes's (*18*) distinction between writerly and readerly texts. Although readerly texts—such as most popular genre fiction—are intended to entertain their mostly passive readers, writerly—or literary—texts engage their readers creatively as writers. Similarly, Mikhail Bakhtin (*19*) defined literary fiction as polyphonic and proposed that readers of literary fiction must contribute their own to a cacophony of voices. The absence of a single authorial perspective prompts readers to enter a vibrant discourse with the author and her characters.

Bruner (*20*), like Barthes and Bakhtin, has proposed that literature engages readers in a discourse that forces them to fill in gaps and search "for meanings among a spectrum of possible meanings" (p. 25). Bruner argues that to elicit

The New School for Social Research, 80 Fifth Avenue, New York, NY 10011, USA.

*Corresponding author. E-mail: kiddd305@newschool.edu (D.C.K.); castanoe@newschool.edu (E.C.)